



ANNUAL  
REVIEWS **Further**

Click [here](#) to view this article's online features:

- Download figures as PPT slides
- Navigate linked references
- Download citations
- Explore related articles
- Search keywords

# Sound Absorption Structures: From Porous Media to Acoustic Metamaterials

Min Yang and Ping Sheng

Department of Physics, Hong Kong University of Science and Technology, Clear Water Bay, Kowloon, Hong Kong, China; email: sheng@ust.hk

Annu. Rev. Mater. Res. 2017. 47:83–114

The *Annual Review of Materials Research* is online at [matsci.annualreviews.org](http://matsci.annualreviews.org)

<https://doi.org/10.1146/annurev-matsci-070616-124032>

Copyright © 2017 by Annual Reviews.  
All rights reserved

## Keywords

porous media, micro-perforated panel, acoustic metamaterials, causality, broadband optimal metamaterial absorber, customized sound absorber, low-frequency sound absorption

## Abstract

The recent advent of acoustic metamaterials has initiated a strong revival of interest on the subject of sound absorption. The present review is based on the physics perspective as the coherent basis of this diverse field. For conventional absorbers, viscous dissipation and heat conduction at the fluid-solid interface, when expressed through micro-geometric parameters, yield an effective medium description of porous media and micro-perforated panels as effectual sound absorbers. Local resonances and their geometric and symmetry constraints serve as the framework for surveying a variety of acoustic metamaterial absorbers that can realize previously unattainable absorption spectra with subwavelength-scale structures. These structures include decorated membrane resonators, degenerate resonators, hybrid resonators, and coiled Fabry-Pérot and Helmholtz resonators. As the acoustic response of any structure or material must obey the causality principle, the implied constraint—which relates the absorption spectrum of a sample to its required minimum thickness—is presented as a means to delineate what is ultimately possible for sound-absorbing structures. The review concludes by describing a recently reported strategy for realizing structures that can exhibit custom-designed absorption spectra, as well as its implementation in the form of a broadband absorber with a thickness that is close to the minimum value as dictated by causality.

## 1. INTRODUCTION

Owing to the importance of sound absorption in room acoustics and environmental noise remediation, its study and practice were extensively pursued during the past century. For sound in the audible frequency range of 20 to 20,000 Hz, dissipation in the transmitting medium—air—is usually minimal so that the effective absorption of sound depends on micro- and/or macrostructured materials in which the sound energy is dissipated through two mechanisms associated with the solid-air interface. One is viscous dissipation in the vicinity of the solid surface, where the non-slip boundary condition can cause large relative motion within the viscous boundary layer. The other is heat conduction through solids, which leads to the breakdown of the adiabatic character of sound propagation. It follows that materials with a large microstructured air-solid interfacial area, e.g., porous media, generally have the largest dissipation coefficients.

Because sound is associated with very small air displacement velocities, its dissipation as a function of frequency must obey the linear response theory, in which the generalized flux (e.g., electrical current density, flow rate, heat flux) is linearly proportional to the generalized force (e.g., gradients of electrical potential, pressure, temperature). Because dissipative force varies linearly as function of the rate (e.g., dynamic friction varies linearly as a function of relative velocity) and dissipated power is given by the product of force and flux, it follows that sound dissipation is a quadratic function of frequency, as shown below. Hence, for low-frequency sound, dissipation is inherently much weaker than for high-frequency sound.

The dissipation coefficient is not the only parameter controlling sound absorption. Dissipated energy is given by the volume integral of the product between the local energy density and the dissipation coefficient. Hence, even if the dissipation coefficient is large, the total absorption can be weak if most of the wave energy is reflected at the structure-air interface. This highlights the importance of impedance matching in sound absorption. Impedance is defined as the product of mass density and sound velocity. Impedance matching with air implies no reflection from the sound-absorbing structure, which guarantees that the maximum amount of sound energy can be subject to absorption inside the structure. To diminish impedance mismatch, porous materials are shaped into wavelength-scale pyramids so as to minimize reflection, usually denoted as the gradient index strategy, and micro-perforated panels (MPPs) use designed backcavities to better impedance match with air over a desired frequency band.

Above are the main elements of physics relevant to sound absorption. They serve as the background for this review, which comprises three parts. The first part is focused on traditional porous materials such as plastic foam, fiber glass, and mineral wool (1, 2), whose absorption characteristics can be accounted for by a unifying effective medium theory. Here MPPs are singled out as a special topic because it utilizes the resonance principle for attaining impedance matching over certain frequency regimes and hence serves as a suitable link to what follows. The second part reviews acoustic metamaterial absorbers that utilize local resonances to enhance the energy density and thereby the sound dissipation. In this context, during the past decade, structures that resonate locally with subwavelength scales (3–9), acoustic metamaterials (10, 11), and metasurfaces (12, 13) have shown diverse functionalities in the manipulation of sound such as negative refraction (14–16), subwavelength imaging (17–19), cloaking (20, 21), and one-way transmittance (22, 23). It is not surprising that some acoustic metamaterial structures can exhibit near-perfect absorption within deep-subwavelength volumes (24–38), far beyond the limit of conventional sound-absorbing materials. The third part reviews the recent advances in achieving optimal sound-absorbing structures. Here optimality is defined by attaining the limit as dictated by the causality constraint, which must be obeyed by acoustic responses of all sound-absorbing structures and materials. We show that broadband optimal metamaterial absorbers (BOMAs) (39, 39a) can be constructed by

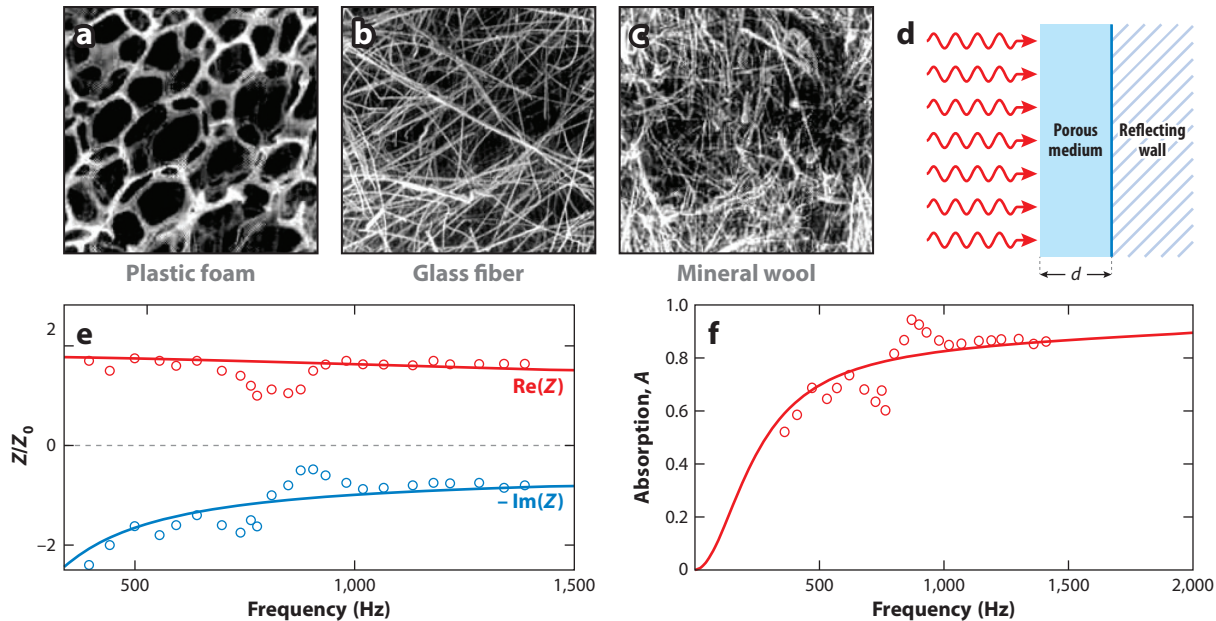


**Figure 1**

Absorption by porous materials. The microstructures of three different porous materials are shown in (a) plastic foam, (b) glass fiber, and (c) mineral wool. Panel *d* shows the measurement geometry for the data on glass fiber shown in panels *e* and *f*. For a sample with  $d = 5.6$  cm,  $\phi = 0.94$ ,  $\kappa_0 = 4.53 \times 10^{-10} \text{m}^2$ ,  $\alpha_\infty = 1.06$ ,  $\Lambda = 0.56 \times 10^{-4}$  m, and  $\Lambda_\tau = 1.1 \times 10^{-4}$  m, the predictions of the effective medium theory (Equation 12) on the real and imaginary parts of the impedance are shown in panel *e*, plotted as a function of frequency. Here the open circles are the measured results, and the solid lines denote the theory predictions. In panel *f*, the measured (*open circles*) and predicted (*solid line*) absorption coefficients are plotted as a function of frequency. The experimental data in panels *e* and *f* are adapted from Allard et al. (40). The photographs in panels *a–c* are adapted with permission from Fahy (100), courtesy of Mr. M.J.B. Shelton.

using a conventional porous medium with carefully designed acoustic metamaterial backing so that flat, near-perfect broadband absorption is achieved starting at a lower cutoff frequency of a few hundred hertz. The sample thickness is close to the minimum thickness as defined by the causality relation; i.e., the structure is close to optimal.

## 2. POROUS SOUND ABSORBERS

As **Figure 1a–c** shows, porous materials usually have two phases comprising a solid framework intertwined with a network of pores. The viscosity and thermal gradient in the vicinity of the solid-air interface result in the dissipation of energy for sound waves. By denoting the sound velocity field by  $\mathbf{v} = v_i$  and the temperature gradient with  $\nabla T$ , the rate of energy dissipation is given by (41, pp. 300–3)

$$\dot{E} = -\frac{\kappa}{T} \int (\nabla T)^2 dV - 2 \int D dV, \quad 1.$$

where  $\kappa$  is the thermal conductivity of air and  $D$  is the air dissipative function

$$D = \eta \left( v_{ik} - \frac{1}{3} \delta_{ik} v_{ll} \right)^2 + \frac{1}{2} \zeta v_{ll}^2. \quad 2.$$

Here  $\eta$  and  $\zeta$  are the shear and bulk viscosity of air, respectively,  $\delta_{ik}$  is the Kronecker delta function, and  $v_{ik} = (\partial v_i / \partial x_k + \partial v_k / \partial x_i) / 2$ . For sound waves of angular frequency  $\omega$  and speed  $v_0$ , Equation 1 can be expressed alternatively in terms of the energy averaged over one oscillation within a volume  $V_0$ ,  $\langle E \rangle = \rho_0 v_0^2 V_0 / 2$ . By using the thermodynamic formula,  $c_p - c_v = T v_0^2 c_v / c_p \cdot (\partial V / \partial T)_p^2 / V_0^2$ , we have (41, pp. 300–3)

$$\langle \dot{E} \rangle = \frac{\omega^2}{\rho_0 v_0^2} \left[ \left( \frac{4}{3} \eta + \zeta \right) + \kappa \left( \frac{1}{c_v} - \frac{1}{c_p} \right) \right] \langle E \rangle. \quad 3.$$

Here  $\rho_0$  is the air density, and  $c_v, c_p$  are the specific heat evaluated at fixed volume and fixed pressure, respectively. The quadratic frequency dependence of the energy dissipation rate is explicitly seen, as stated above. Because the solid frame has a thermal conductivity different from (i.e., usually larger than) that of air, the solid frame temperature can be assumed to stay constant. It follows that, with the adiabatic compression and extension associated with the sound wave, there can be small temperature variations in air that would lead to transient temperature gradients in the vicinity of the air-solid interface. In accordance with the first term of Equation 1, such temperature gradients lead to dissipation. For the second term of Equation 1, the non-slip boundary condition for the air-solid interface means that there is always a viscous boundary layer, with a thickness given by  $l_{\text{vis}} = \sqrt{\eta / (\rho_0 \omega)}$ , within which there can be a significant normal gradient in the tangential air displacement velocity relative to the solid surface, provided pore diameter  $l \gg 2l_{\text{vis}}$ . Such velocity gradients, plus the nonzero divergence of  $\mathbf{v}$ , provide another source of energy dissipation. Of course, for  $l_{\text{vis}} \leq l$  the sound waves would decay in the pores along the direction of propagation.

## 2.1. Parameters Relevant to a Porous Medium

A porous medium is usually characterized by three parameters: porosity, static permeability, and tortuosity.

**2.1.1. Porosity  $\phi$ .** The fraction of the pore volume  $V_f$  filled with air of the total volume  $V_t$  is denoted as the porosity (1, 42)

$$\phi = \frac{V_f}{V_t}. \quad 4.$$

Porosity is a fundamental geometric parameter for porous materials. For acoustic dissipative materials, porosity can be close to 1.

**2.1.2. Static permeability  $\kappa_0$ .** In the limit of  $l_{\text{vis}} \gg l$ , i.e., the static regime, the porous medium is characterized by Darcy's law (43), which governs the air flow rate under a pressure gradient. For a sample with thickness of  $d$ , a pressure difference  $\Delta p$  on two ends of the porous medium would result in a flow velocity given by

$$v = -\frac{\kappa_0}{\eta \phi} \frac{\Delta p}{d}. \quad 5.$$

Here the permeability  $\kappa_0$  is a parameter depending only on the micro-geometry of the porous frame (44–46):

$$\kappa_0 = c \Lambda_\tau^2 f(\phi), \quad 6.$$

where  $c$  is a dimensionless constant,  $\Lambda_\tau = 2V_f / S_f$  is the thermal characteristic length (47),  $S_f$  denotes the frame-air interface area, and  $f(\phi)$  is a function of porosity that is  $\sim \phi^3$  for small  $\phi$  (44).

**2.1.3. Tortuosity  $\alpha_\infty$ .** For airborne sound waves impinging on a porous medium, the pores and the frame represent two parallel channels, with the pores having a much lower impedance. Hence the waves tend to travel mostly in the pores. Because the pores are not straight, the wave is effectively slowed down. This slowdown effect can be quantified by the pores' tortuosity,  $\alpha_\infty$ , defined by the effective arc-chord ratio, i.e., the ratio of the length of the channel length  $L$  to the straight-line distance  $C$  between its two ends (45),

$$\alpha_\infty = \frac{L}{C}. \quad 7.$$

Tortuosity is 1 for a straight channel and is infinite for a closed loop.

## 2.2. Effective Medium Description for Porous Media

A macroscopic description that ignores the fine details of microstructures but focuses on the overall properties of porous media is termed effective medium theory, which uses a set of homogeneous material parameters to effectively characterize sound wave propagation.

In a porous medium, a time harmonic acoustic wave with frequency  $\omega$  must satisfy Newton's law and the constitutive relation:

$$\nabla p_{\text{macro}}(\omega) = -\omega^2 \rho_e(\omega) u_{\text{macro}}(\omega), \quad p_{\text{macro}}(\omega) = -B_e(\omega) \nabla u_{\text{macro}}(\omega). \quad 8.$$

Here  $\rho_e$  is the effective mass density;  $B_e$  is the effective modulus; and  $p_{\text{macro}}$  and  $u_{\text{macro}}$  are the macroscopic sound pressure and displacement field, respectively.

In the model of Johnson et al. (45) and the Champoux-Allard model (48), the effective mass density and modulus can be expressed as

$$\rho_e(\omega) = \rho_0 \alpha(\omega), \quad 9a.$$

$$B_e(\omega) = \frac{\gamma p_0}{\gamma - (\gamma - 1)/\alpha_\tau(\omega)}. \quad 9b.$$

Here  $\gamma$  is air's adiabatic index;  $p_0$  denotes atmospheric pressure; and  $\alpha(\omega)$ ,  $\alpha_\tau(\omega)$  are the dynamic tortuosity and thermal tortuosity, respectively, given by (1)

$$\alpha(\omega) = \alpha_\infty + \frac{i\eta\phi}{\omega\rho_0\kappa_0} \sqrt{1 - \frac{i\omega\rho_0}{\eta} \left( \frac{2\alpha_\infty\kappa_0}{\Lambda\phi} \right)^2}, \quad 10a.$$

$$\alpha_\tau(\omega) = 1 + \frac{i8\kappa}{\omega\rho_0 c_p \Lambda_\tau^2} \sqrt{1 - \frac{i\omega\rho_0 c_p}{\kappa} \left( \frac{\Lambda_\tau}{4} \right)^2}. \quad 10b.$$

Here  $\Lambda = 2 \int_{V_f} v_{\text{inviscid}}^2 dV / \int_{S_f} v_{\text{inviscid}}^2 dS$  is the viscous characteristic length, with  $v_{\text{inviscid}}$  being the air velocity field in the absence of viscosity (47). The dynamic tortuosity  $\alpha(\omega)$  in Equation 10a expresses the effects of air viscosity on the effective mass density, whereas the thermal tortuosity  $\alpha_\tau(\omega)$  in Equation 10b reflects the influence of thermal conduction on the effective bulk modulus.

By taking into account the elastic deformation of the solid frame, Von Terzaghi (49) and Biot (50) presented a theoretical model for sound propagation in porous materials saturated with a viscous fluid. The theory was further generalized to anisotropic materials as well as to cases involving viscoelastic frames (51). Biot's dynamic theory was published in two articles (52, 53), in which three types of waves were identified: two longitudinal waves and one shear wave. The two types of longitudinal waves of Biot are distinguished by the in-phase and out-of-phase oscillations of the

fluid relative to the solid frame. Other models used to predict the behaviors of porous materials based on empirical laws include those developed by Delany & Bazley (54) and Allard & Champoux (55). Recently, based on the analogy to electromagnetism, Lafarge & Nematı proposed an effective medium theory allowing spatial dispersion. This theory delineates nonlocal correlations in composite media for sound waves propagating in porous structures (56, 57).

For airborne sound impinging on a porous medium, the solid frame motion can largely be ignored, and the predictions of the effective medium theory are testable by comparison with the experimental results. For a layer of porous material with thickness  $d$  backed by a reflecting wall, the reflection coefficient can be evaluated from the surface impedance  $Z$  as

$$R = \frac{Z - Z_0}{Z + Z_0}. \quad 11.$$

Here  $Z_0$  denotes the air impedance, given by  $Z_0 = \rho_0 v_0$ , where  $v_0 = 343$  m/s and  $\rho_0 = 1.2$  kg/m<sup>3</sup>, and the surface impedance can be expressed in terms of the effective parameters:

$$Z(\omega) = i\sqrt{\rho_e B_e} \cot(\omega d \sqrt{\rho_e/B_e}). \quad 12.$$

The sound absorption coefficient is calculated as  $A = 1 - |R|^2$ .

The validity of Equation 9 was confirmed by the experiment of Allard et al. (40), as shown in **Figure 1d–f**. A layer of 5.6-cm-thick sample made of glass wool was placed on top of a rigid substrate. The surface impedance (Equation 12) evaluated from the measured reflection  $R$  is shown in **Figure 1e**. Solid curves are the theory predictions based on Equation 12, in which the effective mass density and bulk modulus are calculated by using Equation 9 with the parameter values of glass wool given by  $\phi = 0.94$ ,  $\kappa_0 = 4.53 \times 10^{-10}$  m<sup>2</sup>,  $\alpha_\infty = 1.06$ ,  $\Lambda = 0.56 \times 10^{-4}$  m, and  $\Lambda_\tau = 1.1 \times 10^{-4}$  m. Good agreement between theory and experiment is seen. The small ripple around 850 Hz is the consequence of resonant motions of the glass framework. Because Equation 9 is based on the assumption of a rigid framework, it cannot predict this effect. The absorption behavior of this porous material is shown in **Figure 1f** on the basis of the prediction from Equation 12. Absorption displays a relatively flat absorption coefficient of >80%, starting from 800 Hz.

### 2.3. Perforated and Micro-Perforated Panel Absorbers

The perforated panel can be treated as a special version of porous material, comprising a thin, rigid (usually metallic) plate with straight holes, as illustrated in **Figure 2a**. In practice, such structures have been used as facings for porous materials to improve low-frequency absorption (59–62; 63, pp. 460–63). In the 1960s and 1970s, Maa (58, 64) realized that if the cross-sectional scale of the perforated pores is in the submillimeter range—in contrast to conventional ones, which are in the millimeter range—then such MPPs can exhibit large absorption in the low-frequency regime.

As perforated panels have a relatively simple geometry, an accurate theoretical model is available. For a rigid plate of thickness  $\tau$ , pore diameter  $l$ , and overall porosity  $\phi$ , the acoustic effect of the perforated plate can be characterized by its impedance, defined as the ratio between the pressure drop across its two surfaces,  $\Delta p$ , and the surface-averaged air velocity through the holes,  $\bar{v}$ . According to Maa (58), the impedance is given by

$$Z \equiv \frac{\Delta p}{\bar{v}} = -i\omega \frac{\rho_0 \tau}{\phi} \left[ 1 - \frac{2}{\sigma \sqrt{i}} \frac{J_1(\sigma \sqrt{i})}{J_0(\sigma \sqrt{i})} \right]^{-1} - i0.85\omega \frac{\rho_0 l}{\phi}, \quad 13.$$

with the dimensionless  $\sigma = l\sqrt{\omega\rho_0/(4\eta)}$ , where  $J_{0(1)}$  denotes the Bessel function of zeroth (first) order. Here the first term is from air's viscous motions in straight pores, first obtained by Lord

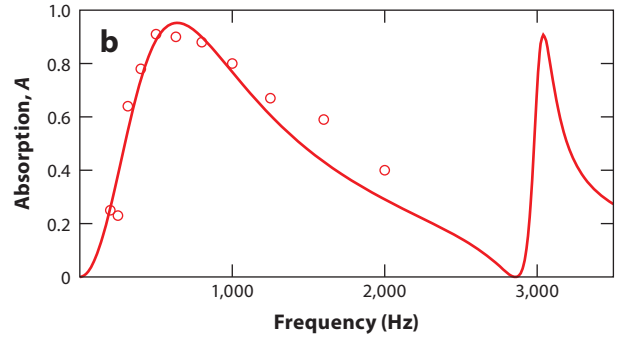
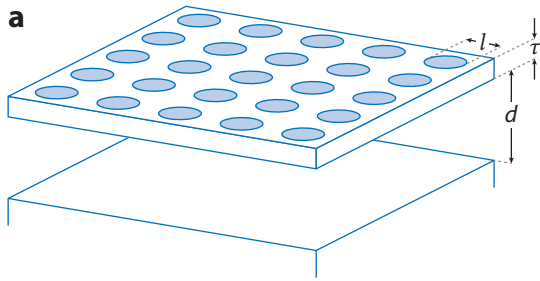


**Figure 2**

Micro-perforated panel (MPP) absorber. (a) Schematic illustration for the structure of an MPP. Here  $\tau$  denotes the thickness of the perforated plate,  $l$  denotes the diameter of the circular perforated holes, and  $d$  denotes the back cavity thickness. For ease of visualization, the size of the holes is greatly exaggerated. (b) The absorption coefficient of an MPP with  $\tau = l = 0.2$  mm,  $\phi = 0.5\%$ , and  $d = 6$  cm. Here  $\phi$  is the porosity of the perforated plate, given by the total area of the circular holes divided by the total area of the plate. The solid curve is the prediction from Maa's theory (Equation 13), and the open circles are data adapted from Maa (58).

Rayleigh (65) and Crandall (66), and the second term is a correction arising from the piston sound radiation at the pores' ends suggested by Morse & Ingard (61; 63, pp. 460–63). For MPPs, the value of  $\sigma$  is generally in the range between 1 and 10, and a handy approximation to Equation 13 is given by

$$Z = -i\omega \frac{\rho_0 \tau}{\phi} \sigma_i + \frac{32\eta\tau}{\phi l^2} \sigma_r, \quad 14.$$

in which

$$\sigma_i = 1 + 1/\sqrt{1 + \frac{\sigma^2}{2}} + 0.85 \frac{l}{\tau}, \quad \sigma_r = \sqrt{1 + \frac{\sigma^2}{32}} + \frac{\sqrt{2}}{32} \sigma \frac{l}{\tau}. \quad 15.$$

The sound absorption performance of an MPP can be enhanced by placing it in front of a cavity with a reflecting wall that is a distance  $d$  away. The air cavity serves the function of enhancing the wave amplitude (and hence the energy density) in the plate through the constructive interference effect. The impedance for the composite system is given by

$$Z_c = Z + iZ_0 \cot(\omega d/v_0), \quad 16.$$

from which the reflection coefficient  $R = (Z_c - Z_0)/(Z_c + Z_0)$  and the absorption coefficient  $A = 1 - |R|^2$  for normal incident sounds can be evaluated.

**Figure 2b** shows an example of MPP absorption (58), in which  $\tau = l = 0.2$  mm,  $\phi = 0.5\%$ , and  $d = 6$  cm. An absorption peak close to 0.9 can be seen at approximately 760 Hz, followed by near-zero absorption at approximately 2,850 Hz. A second absorption peak is at 3,050 Hz. Such behavior is distinct from the absorption spectrum of a layer of porous material as shown in **Figure 1f**. The reason for this difference is due to the constructive interference of the back-reflected wave with that of the incident wave inside the thin layer of perforated plate. Such resonance usually takes the Lorentzian form as a function of frequency. For frequencies in between two adjacent resonances, destructive interference can occur at the so-called antiresonance frequency, at which the responses of the two resonances may completely cancel each other. In the present case, antiresonance occurs at 2,850 Hz. Recent works on improving the absorption of MPP by altering the resonant features of the back chambers include those of Liu & Herrin (67), Wang and colleagues (68, 69), and Park (70).

### 3. METAMATERIAL ABSORBERS

Metamaterials are characterized by local resonators that are subwavelength in scale. Because resonances would enhance the energy density, metamaterials are potential absorbers, even though high absorption would necessarily occur only in the vicinity of resonant frequencies. Hence metamaterial absorbers are inherently narrow band in nature. In this section, we describe the metamaterial sound absorbers from a perspective of vibrational symmetry and geometric constraint.

#### 3.1. Elastic Membrane as Sound Absorber

A decorated membrane (DM) comprises a pretensioned elastic membrane with a rigid weight(s) adhered on its surface. Due to the small restoring force of DM, resonances can easily be in the audible range. As first reported by Yang et al. (71), a circular DM that is 20 mm in diameter and 0.28 mm in thickness has its lowest resonance at 146 Hz. The relevant airborne sound at this frequency has a wavelength of 2.35 m; i.e., the size of a DM can be in the extreme subwavelength regime.

Vibration of a DM can be characterized by its normal displacement velocity,  $v(\mathbf{x})$ , where  $\mathbf{x}$  denotes the lateral coordinates. By denoting the surface-averaged displacement velocity by  $\bar{v}$ , the component that is left over,  $\delta v(\mathbf{x}) = v(\mathbf{x}) - \bar{v}$ , denoted the delta component, can couple only to the evanescent waves. This is because from the dispersion relation of airborne sound we have  $|\mathbf{k}_{\parallel}|^2 + k_{\perp}^2 = (2\pi/\lambda)^2$ , where the subscripts  $\parallel$  and  $\perp$  denote the vector components parallel and perpendicular to the membrane surface, respectively. The continuity of normal displacement means that the air displacement next to the membrane's surface is the same as that of the membrane. Owing to the subwavelength lateral scale of the membrane, the magnitude of  $\mathbf{k}_{\parallel}$  in the Fourier transform of  $\delta v(\mathbf{x})$  must be larger than  $2\pi/\lambda$ , hence  $k_{\perp}^2 < 0$ ; i.e., the wave must be evanescent along the perpendicular direction. In contrast, the  $\mathbf{k}_{\parallel}$  components for  $\bar{v}$  peak at  $\mathbf{k}_{\parallel} = 0$ , and hence  $\bar{v}$  couples to the propagating modes. It follows that in the far field, the piston-like motion represented by  $\bar{v}$  is sufficient to characterize the scattering characteristics of DM, and an effective impedance can be defined by  $Z \equiv \Delta p/\bar{v}$ , with  $\bar{v}$  being the DM's displacement velocity when a pressure difference,  $\Delta p$ , is applied across its two surfaces.

The effective impedance is dispersive, as it is related to the resonances of DM (72) such that  $Z = i/(\omega g)$ , where  $g$  is the surface-averaged Green function, defined as the ratio between the averaged displacement,  $\bar{u}$ , and  $\Delta p$ :

$$g = \frac{\bar{u}}{\Delta p} = \sum_n \frac{|\bar{u}_n|^2}{\rho_n(\Omega_n^2 - \omega^2 - 2i\omega\beta_n)}. \quad 17.$$

Here  $\rho_n \equiv \int \rho |u_n|^2 dV$  is the displacement eigenfunction-weighted mass density for DM's  $n$ th mode  $u_n$  with a resonance frequency  $\Omega_n$ , and  $\rho$  is the local density. If we denote the viscosity coefficient of the system to be  $\eta$ , then the dissipation coefficient  $\beta_n$  in Equation 17 is defined as

$$\beta_n = \int \eta |\nabla u_n|^2 dV / (2\rho_n). \quad 18.$$

For a plane wave incident on a DM, the normalized transmission amplitude  $T$  and reflection amplitude  $R$  can be evaluated from the impedances as

$$R = \frac{Z}{2Z_0 + Z}, \quad T = \frac{2Z_0}{2Z_0 + Z}. \quad 19.$$

In arriving at the above expressions, we note that the geometric constraint as detailed below is already incorporated. In terms of the impedances, the sound dissipation coefficient  $A = 1 - |R|^2 - |T|^2$  is given by

$$A = \frac{4Z_0 \operatorname{Re}(Z)}{[2Z_0 + \operatorname{Re}(Z)]^2 + \operatorname{Im}(Z)^2}. \quad 20.$$

The maximum absorption,  $A_{\max} = 0.5$ , occurs when  $\operatorname{Re}(Z) = 2Z_0$  and  $\operatorname{Im}(Z) = 0$ , known as the critical coupling condition (73, 74). When that happens,  $R = T = 0.5$ . According to Equation 17, this condition is possible only at DM's resonance with just the right amount of dissipation.

Mei et al. (25) reported high sound absorption by a thin DM; Yang et al. (24) and Chen et al. (75, 76) investigated its upper bound. As shown in **Figure 3a**, a rectangular membrane was stretched and fixed on its four edges. Two semicircular metallic platelets were attached, facing

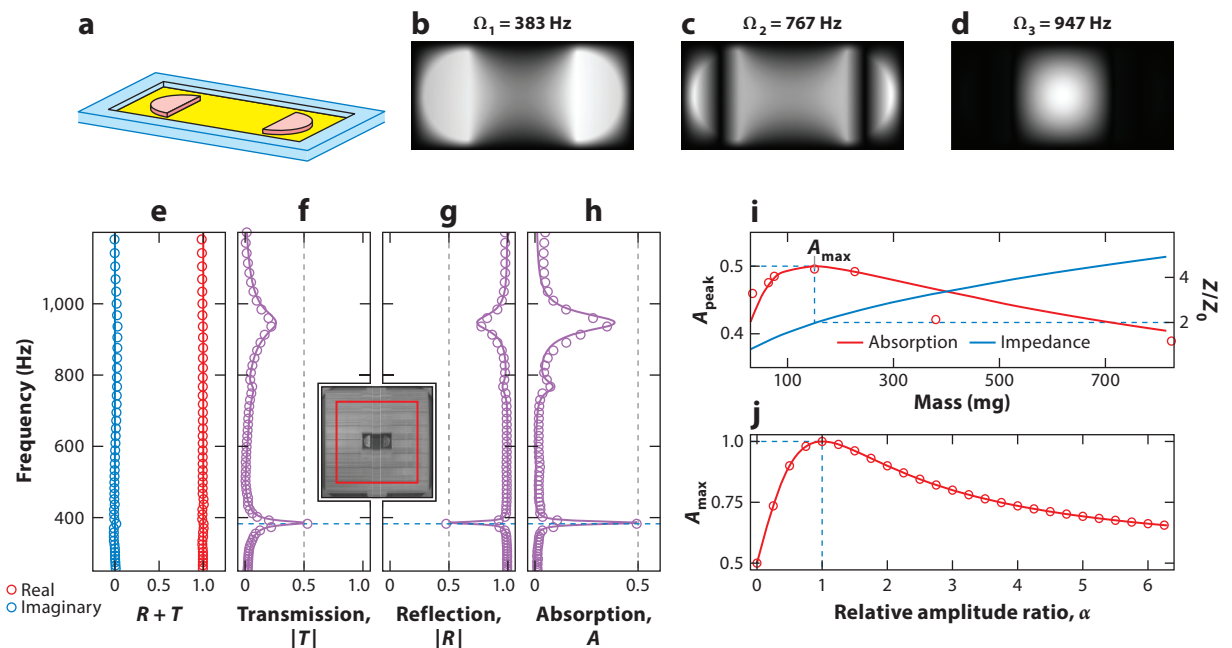


**Figure 3**

Absorption by a decorated membrane (DM) resonator. (a) Schematic illustration of a DM comprising two semicircular platelets (pink) adhered onto a rectangular membrane (yellow) and facing each other. The elastic membrane is fixed on the supporting frame (blue). (b–d) The three resonant eigenmodes of the DM shown in panel a that are responsible for the three absorption peaks. Light indicates large normal displacement, and dark indicates small displacement. In panel b, the large displacements are localized on the platelets, which execute a flapping motion, with the diameter of the semicircular platelet acting as the center of rotation, simultaneous with the large normal translational motion. In panel c, the membrane between the two platelets displays a large displacement. The two platelets flap, but without the large translational displacement. In panel d, all the displacement is localized on the central part of the membrane. (e–h) The measured transmission, reflection, and absorption coefficients when waves are incident from one side. An image of the sample is shown in the inset, where the red square indicates the cross section of the impedance tube. At 383 Hz, maximum absorption of 50% occurs, and  $R = T = 0.5$ , as predicted by Equation 19, a result of the continuity of displacement velocity on two sides of the thin membrane. (i) The first peak absorption coefficient (red curve) of the DM plotted as a function of the mass of the platelets. The associated surface impedance is denoted by the blue curve. Here the open circles are measured data, adapted from Yang et al. (24), and the solid curve represents the theory. At a maximum absorption of 50%, the associated impedance is exactly twice that of air. (j) Absorption of the DM when waves are incident from two sides, plotted as a function of the relative amplitude ratio  $\alpha$  between the two incident waves. Maximum total absorption occurs at  $\alpha = 1$ , i.e., when the coherent perfect absorption (CPA) condition is satisfied. Here the open circles are numerical simulations, and the solid line the theory prediction. Adapted from Reference 24.

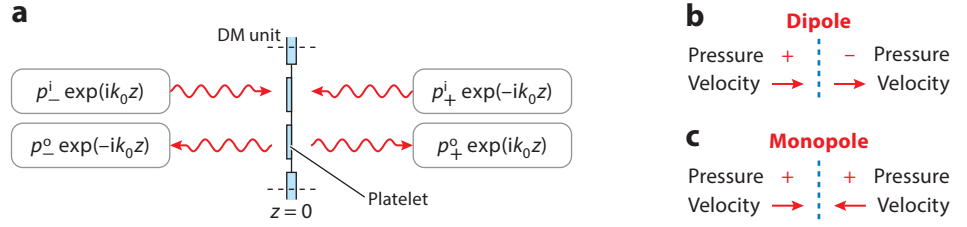


**Figure 4**

Dipole and monopole resonances. (a) Schematic illustration of the incident and scattered waves from a decorated membrane (DM). The subscripts + and – are indicative of the right side and left side of the DM, and the superscripts i and o denote the incoming and outgoing waves, respectively. Here  $k_0$  is the acoustic wave vector in air. (b) Illustration of the relevant waves, among those shown in panel a, that are consistent with the symmetry of the dipole resonance. (c) Illustration of the relevant waves, among those shown in panel a, that are consistent with the symmetry of the monopole resonance.

each other. The membrane had a width of 15 mm, a length of 30 mm, and a thickness of 0.2 mm. The radius of each platelet was 6 mm, whereas its mass could vary for different samples. The surface impedance of its first resonance, i.e., the first absorption peak, could be tuned by changing the platelet mass. **Figure 3i** shows that the maximum absorption for the first resonance was achieved when all the samples had identical platelet masses of 151 mg, at which the condition  $Z = 2Z_0$  was satisfied. Both  $R$  and  $T$  are approximately equal to 0.5 at the resonant frequency of 383 Hz, in agreement with Equation 19, and the absorption coefficient reached its maximum value  $A_{\max} = 0.5$  (**Figure 3f–b**). Chen et al. (75, 76) further proposed a complete analytical model for such DM absorption behavior and confirmed the energy absorption limit. As seen below, this absorption upper bound is the result of a very general geometric constraint.

### 3.2. Geometric Constraint and a Conservation Law

Due to the fact that the membrane is very thin, time harmonic variation of its thickness can occur only at very high frequencies. Hence at audible frequencies we can assume the membrane thickness to be constant. It follows that the membrane's surface velocity  $\bar{v}_- = \bar{v}_+$ , where the subscript – (+) denotes the left-hand (right-hand) side of the membrane. Let us consider two incoming sound waves counterpropagating from two sides, impinging on the membrane with complex pressure amplitudes  $p_-^i$  and  $p_+^i$  (**Figure 4a**) and scattering into two outgoing waves with complex pressure amplitudes  $p_-^o$  and  $p_+^o$ . Here the superscripts i and o denote incoming and outgoing waves, respectively, and  $p_{+(-)}^{i(o)}$  denotes the sound wave pressure modulation with respect to the constant ambient pressure. From the definition of impedance, the surface-averaged air velocity next to the left-side membrane surface is given by  $\bar{v}_- = (p_-^i - p_-^o)/Z_0$ , and that for the right side is  $\bar{v}_+ = (p_+^o - p_+^i)/Z_0$ . From displacement continuity at the air-membrane interface, it follows that  $\bar{v}_- = \bar{v}_+$  implies

$$p_m = p_m^i = \frac{1}{2}(p_-^i + p_+^i) = \frac{1}{2}(p_-^o + p_+^o) = p_m^o. \quad 21.$$

Equation 21 is a conservation law analogous to the conservation of center of mass momentum in the collision of two equal mass particles. It follows from this analogy that the center of mass energy flux, given by

$$j_m = p_m^2/Z_0, \quad 22.$$

is also conserved and is therefore not available to be dissipated. In this analogy, impedance plays the role of particle mass.

### 3.3. Dipole and Monopole Resonances

Resonances can in general be categorized either as dipole in character, in which the relevant motions are antisymmetric under the mirror reflection on its central plane (as shown in **Figure 4b**), or as monopole in character, in which the motions are symmetric under mirror reflection (**Figure 4c**). Such division is useful because the dipolar motions of a resonator are decoupled from the monopole component, and hence their energies can be independently accounted for (24).

A resonance with a particular symmetry can be excited only if the excitation waves have the same symmetry component. In this respect,  $p_m$  as defined by Equation 21 is monopole in character, and to complete the picture we define

$$p_d = \frac{1}{2}(p_+^i - p_-^i) \quad 23.$$

as the dipolar component of the incident waves. By using the monopole and dipole division, one can immediately deduce that the energy available for dissipation is given by

$$\frac{1}{2Z_0} [(p_+^i)^2 + (p_-^i)^2 - 2p_m^2] = \frac{1}{4Z_0} (p_+^i - p_-^i)^2 = p_d^2/Z_0 = j_d. \quad 24.$$

Hence the absorption coefficient for the DM absorber is given by  $A = j_d/(j_m + j_d)$ . For waves incident from one side only,  $p_+^i = 0$  so that  $j_m = j_d$ , and the absorption upper bound is 50%.

In contrast to the DM, in which only dipole resonances occur at audible frequencies, resonators like Helmholtz resonators (HRs) on a sidewall of a ventilated channel (29, 34), a pair of coupled DMs (33), or air bubbles in rubber (32, 77–79) can exhibit monopolar resonances. If dipole resonances cannot be excited at the relevant frequency regime, then  $j_d$  is the conserved component, and the energy available for absorption is the monopolar component  $j_m$ . A similar 50% absorption upper bound applies in the one-side incident scenario. Merkel et al. (34) experimentally demonstrated this maximum absorption by two sidewall HRs mounted opposite to each other on two sides of a ventilated tube (as shown in **Figure 5a**), in conjunction with an analysis of critical coupling in the complex frequency plane. Coupled through near fields, these two HRs present a hybrid resonance at  $f_0 = (f_2^{\text{HR}} - f_1^{\text{HR}})/2$ , as shown in **Figure 5c**, in which  $f_1^{\text{HR}}$  and  $f_2^{\text{HR}}$  are the two resonance frequencies of the HRs. By tuning the frequency difference  $f_2^{\text{HR}} - f_1^{\text{HR}}$  while keeping  $f_0$  unchanged, the absorption has a maximum of 50%, as shown in **Figure 5d**. In the investigation of the absorption of waterborne sounds by air bubbles in soft solid medium (as shown in **Figure 5b**), Leroy et al. (32) demonstrated that the monopolar motions of bubbles absorb sound with an upper limit of 50% (as shown in **Figure 5e,f**).

An absorption upper bound also exists in nonlinear acoustic systems, as shown by Achilleos et al. (80) in HRs with very high sound intensities, as well as in electromagnetic wave absorption, e.g., laser absorption in thin film structures (81–83).

### 3.4. Coherent Perfect Absorption

By eliminating the monopole component in incoming waves, i.e., by introducing counterpropagating waves on both sides such that  $p_-^i = -p_+^i$  so  $p_m = 0$ , absorption can exceed 50%. In general, for a given ratio  $\alpha = |p_+^i|/|p_-^i|$ , the maximum absorption always occurs when  $p_-^i$  and  $p_+^i$

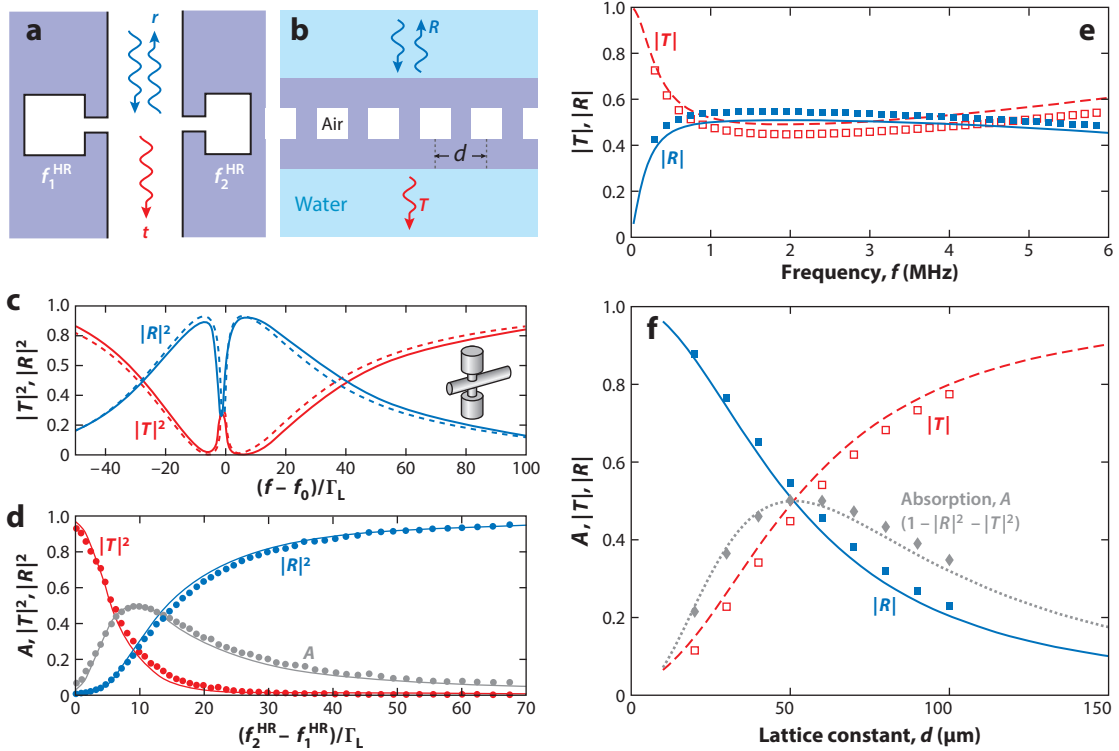


**Figure 5**

Absorption by monopole resonators. (a) Schematic illustration of a pair of coupled Helmholtz resonators (HRs) installed on two sides of an air channel. The two HRs have resonance frequencies at  $f_1^{\text{HR}}$  and  $f_2^{\text{HR}}$ . They are coupled through near field of the sound waves (as the channel width is smaller than the wavelength). As a result, a hybrid resonance appears at  $f_0 = (f_2^{\text{HR}} - f_1^{\text{HR}})/2 = 311$  Hz.

(b) Schematic illustration of a composite absorber for waterborne sounds consisting of air bubble lattices (delineated by *white squares*) with lattice constant  $d$ , embedded in a soft solid medium (*blue*). (c) Transmitted and reflected energy spectra at the maximum absorption condition for the coupled HRs as illustrated in panel a. Here  $\Gamma_L = 3.14$  Hz, the solid curves are data, and dashed curves are theoretical predictions. (d) By tuning the frequency difference  $f_2^{\text{HR}} - f_1^{\text{HR}}$  while keeping  $f_0$  unchanged, the maximum absorption of 50% is seen at  $(f_2^{\text{HR}} - f_1^{\text{HR}})/\Gamma_L = 9.8$ . The relevant scattering spectrum is shown in panel c. The dots are data, and the solid curves are theoretical predictions. Panels c and d adapted with permission from Merkel et al. (34). (e) The transmission and reflection spectra of the composite waterborne sound absorber illustrated in panel b, obtained at the maximum absorption condition. (f) By tuning the lattice constant  $d$  of embedded bubbles, the absorption reaches a maximum of 50%. The solid curves are from theory, and the symbols are from finite element simulations. Panels e and f adapted with permission from Leroy et al. (32).

are opposite in phase so that (as shown in **Figure 3j**)

$$A_{\max} = \frac{j_d}{j_m + j_d} = \frac{(p_-^i)^2 + (p_+^i)^2 + 2|p_-^i p_+^i|}{2(p_-^i)^2 + 2(p_+^i)^2} = \frac{1}{2} + \frac{\alpha}{1 + \alpha^2}. \quad 25.$$

When  $\alpha = 1$ , we have the antisymmetric coherent perfect absorption (CPA) scenario (29). To completely absorb incident sound from one side, the CPA strategy is to use a control wave with the same amplitude but opposite phase, counterpropagating from the other side, so that the transmitted (reflected) wave of the incident sound can be completely canceled by the reflection (transmission) of the control wave through interference. Wei et al. (29) and Yang et al. (84) theoretically predicted and numerically confirmed such antisymmetric CPA by decorated elastic

membranes. Such an antisymmetric CPA effect was recently experimentally realized by Meng et al. (38).

To perfectly absorb sound incident from one side with a monopole resonator, symmetric CPA requires a control wave incoming from the opposite direction with the same phase. Symmetric CPA by HRs was numerically simulated by Wei et al. (29) and was experimentally realized by Meng et al. (38). Song et al. (30) extended the CPA concept to two dimensions with higher-order symmetries such as quadrupole and octupole resonances.

### 3.5. Sound Absorption by Degenerate Resonators

Instead of introducing control waves, another approach to absorb sound effectively is to create a composite resonator comprising a pair of dipole and monopole resonators with the same resonant frequency, i.e., degenerate, and with each satisfying the critical coupling condition.

To characterize the response of such a degenerate pair, we define the dipolar impedance  $Z_d$  for dipole resonators as  $Z_d = p_d/\bar{v}_d = (p_+ - p_-)/(\bar{v}_+ + \bar{v}_-)$ , which is half of the effective impedance we defined for DM, and the monopolar impedance  $Z_m$  for monopole resonators as  $Z_m = p_m/\bar{v}_m = (p_+ + p_-)/(\bar{v}_+ - \bar{v}_-)$ . The absorption coefficient for one-side incident sound waves is then given by

$$A = \frac{2Z_0\text{Re}(Z_m)}{[Z_0 + \text{Re}(Z_m)]^2 + \text{Im}(Z_m)^2} + \frac{2Z_0\text{Re}(Z_d)}{[Z_0 + \text{Re}(Z_d)]^2 + \text{Im}(Z_d)^2}, \quad 26.$$

which comprises two terms from the monopolar and dipolar resonances, respectively. Each term reaches a maximum of 50% when the critical coupling condition,  $Z_m = Z_0 = Z_d$ , is satisfied.

In actual practice, the monopole resonator can be realized in the channel geometry by placing a DM dipole resonator on the channel sidewall backed by a cavity, as shown in **Figure 6a**. When this DM vibrates in and out from the channel sidewall, it pushes (out) and sucks (in) the air in front of the DM, leading to a monopole-like air movement parallel to the channel wall.

As shown in **Figure 6a-f**, by using a DM as the dipole and a sidewall cavity sealed by another DM as the monopole, a degenerate, perfect absorber was experimentally realized at 285.6 Hz within a space that is one order of magnitude smaller than the relevant airborne sound wavelength (33). The relevant physics can be easily described as follows. Total absorption must occur if both transmission and reflection are suppressed. Here the reflection is suppressed by impedance matching, and the transmission is suppressed by destructive interference between the two DMs, one on the sidewall acting as the monopole and the other one perpendicular to the sidewall DM acting as the dipole. By synchronizing the pushing of the air in one with the sucking of the air in the other, the air pressure modulation in the far-field transmission direction is suppressed. Thus, total absorption occurs. In this particular case, the dipole DM does not cover the whole cross section of the air channel; i.e., the channel is ventilated. Hence the air constitutes the third component of the setup, and the dipole plus air behaves as a Fano resonance. As a result, the dipole resonance has to be tuned to a frequency slightly higher than that of the monopole so as to make total absorption occur. This is seen in **Figure 6b,c**. In panels *d*, *e*, and *f* of **Figure 6**, the measured and simulated  $R$ ,  $T$ , and absorption coefficient are shown, respectively. Another sample, with DM as the dipole resonator and a pair of coupled DMs (sealing a thin cavity in between) as the monopole resonator, has also shown similar absorption behavior in a space that is 20 times smaller than the airborne wavelength (**Figure 6g**). In this case, the cross-sectional area of the air channel was completely covered by the combined setup. Hence the dipole and monopole resonances are exactly degenerate. Panels *b-l* of **Figure 6** show results similar to those of the ventilated case. Piper et al. (85) reported the electromagnetic analog of this degenerate resonator absorber.

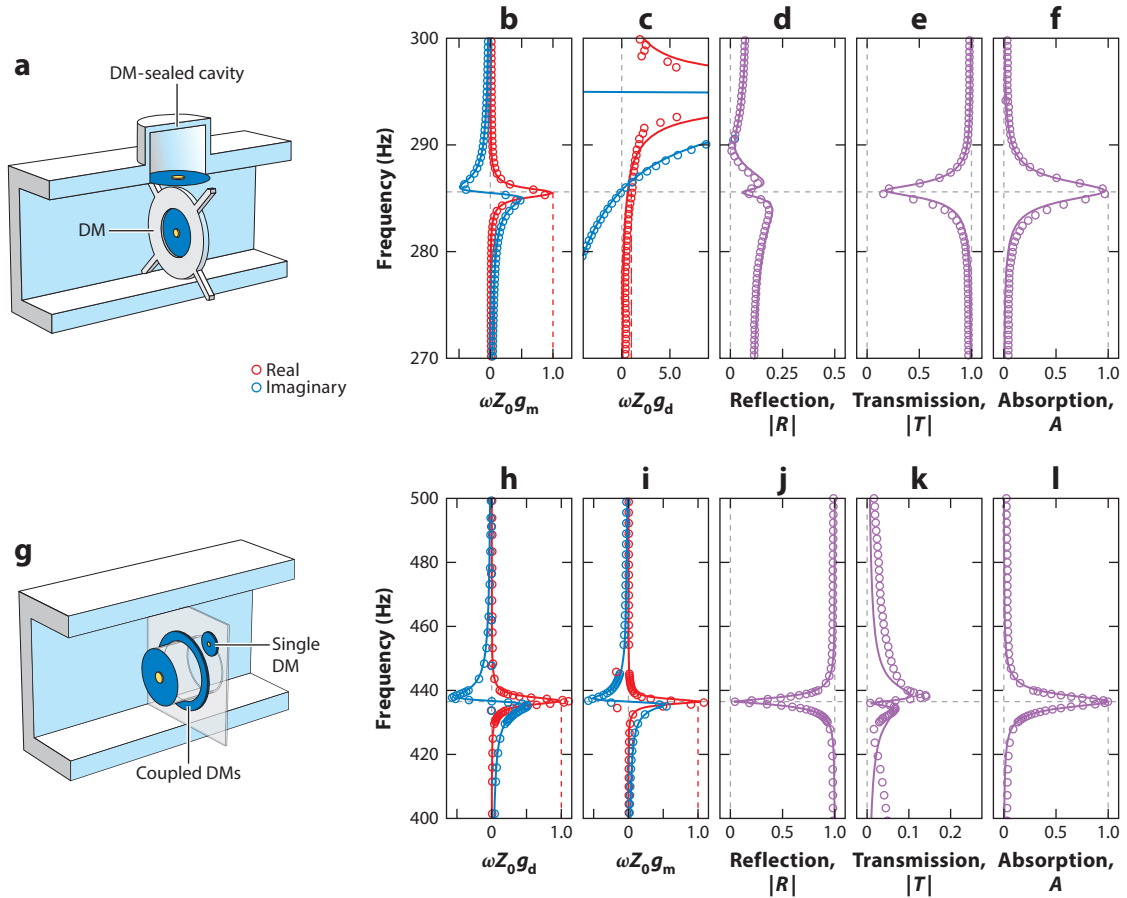


**Figure 6**

Absorption by degenerate resonators. Panel *a* schematically illustrates a ventilated composite absorber comprising a sidewall monopolar resonator placed in the vicinity of a dipolar resonator. The dipole resonator does not cover the whole cross-sectional area of the air channel. As a result, the air contributes to this ventilated setup as the third component, and the dipole resonance is Fano like, owing to the continuum background contributed by the air component. Thus, the dipole and monopole are not exactly degenerate, as can be seen in panels *b* and *c*, in which the renormalized, dimensionless response functions  $g_{d(m)} = i/[\omega Z_{d(m)}]$  for the dipole/monopole absorber are plotted as a function of frequency. Here the open circles represent experiment, and the solid curves are the numerically simulated results. Panels *d*, *e*, and *f* show the relevant reflection, transmission, and absorption coefficients, respectively. Again, the open circles are the measured data, and the solid curves the simulated results. Panel *g* shows a schematic illustration of a flat-panel composite absorber. Here the composite absorber covers the whole cross section of the air channel, and the dipole and monopole resonances are exactly degenerate, as shown in panels *b* and *i*. In panels *j*, *k*, and *l*, the reflection, transmission, and absorption coefficients of the composite absorber are plotted as a function of frequency, respectively. The solid curves are from numerical simulations, and the open circles denote the measured data. DM denotes decorated membrane. Figure adapted from Yang et al. (33).

### 3.6. Hybrid Resonance Absorption

By placing a reflecting wall behind a DM, separated by a distance  $d$ , multiple reflections between the membrane and the reflecting wall (see **Figure 7a,c**) can create a new hybrid resonance (26), with the resulting absorption coefficient for a one-side incident wave reaching nearly 100%. Here, we analyze this multiple-scattering process and the perfect absorption condition with the aid of  $p_m$  conservation as introduced in Section 3.2.

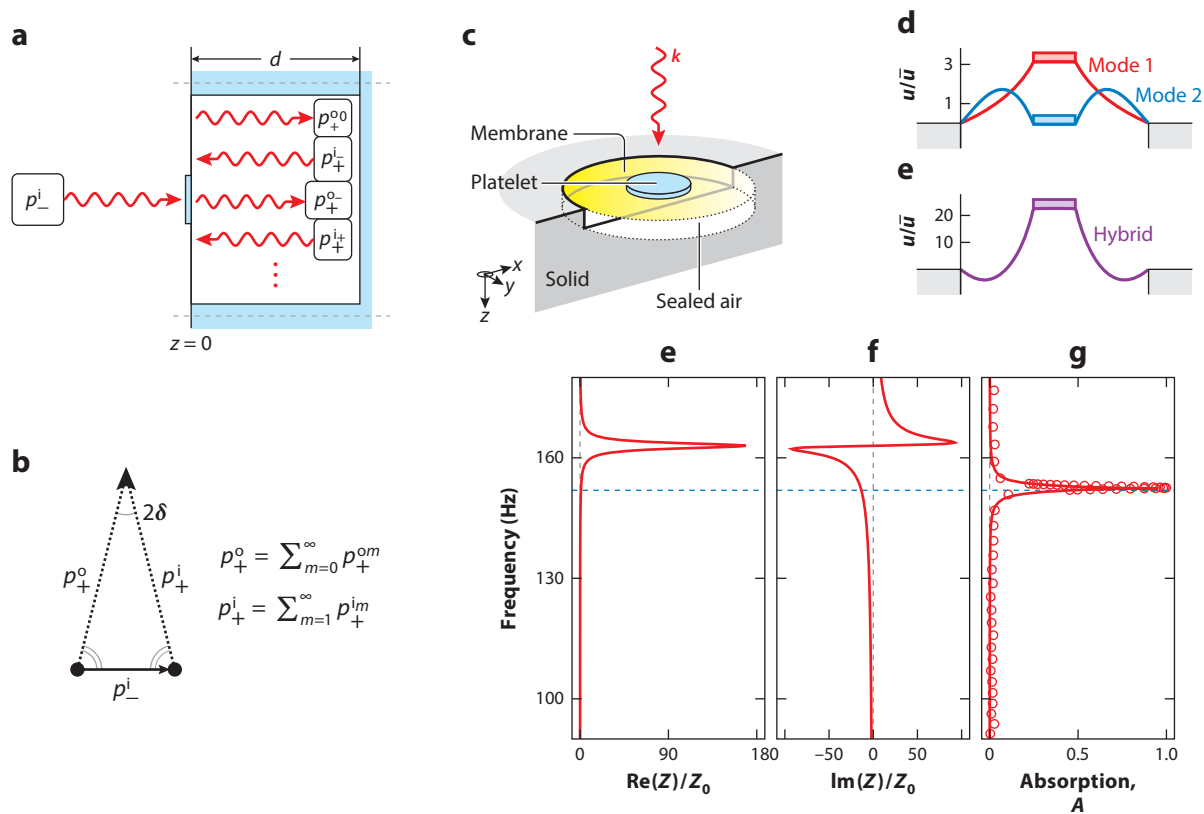


**Figure 7**

Multiple scatterings and sound absorption by hybrid resonance. (a) Schematic illustration of the multiple scatterings introduced by placing a reflecting wall behind a decorated membrane (DM). Here the aim is to find the required DM impedance for total absorption; hence it is assumed that there is no reflected wave. (b) The relevant phasor diagram for the complex pressure amplitudes on two sides of the DM that form an isosceles triangle due to the conservation law imposed by the continuity of displacement velocity on two sides of the DM. The angle between two equal sides of the triangle is given by  $2\delta = 2k_0d$ , owing to the nodal condition at the reflecting wall. (c) Schematic illustration of a hybrid DM absorber. (d) Profiles of the first two eigenmodes of the DM across the diameter of the DM. Here  $u$  denotes the membrane normal displacement, and  $\bar{u}$  denotes its average over the surface of the membrane. The flat rectangle denotes the rigid platelet decorated on the membrane. (e) The hybrid resonance profile of the absorber, in terms of its normal displacement  $u/\bar{u}$ , plotted across the diameter of the DM. Comparing the normal displacement profile to that shown in panel d makes clear that the hybrid mode has a vibrational profile that is a linear superposition of the first two modes. However, the amplitude of the hybrid mode is at least an order of magnitude larger than that of the two original resonances under the same-amplitude incident wave excitation. Panels e and f show the calculated real and imaginary parts of the impedance, respectively, normalized by that of air,  $Z_0$ . At the DM's antiresonance frequency of 161 Hz, the real part of the impedance is very large, more than two orders of magnitude larger than that of air, whereas the imaginary part displays dispersion. However, at the hybrid resonance frequency of 152 Hz (indicated by the blue dashed line), which is a resonance caused by the combined effect of the DM plus the sealed cavity, the DM's real part of impedance is small, whereas the imaginary part is fairly large and negative. The latter is required to cancel the large and positive imaginary impedance from the back-reflecting wall, so the net effect is a combined impedance of the hybrid resonator that is real and close to that of air. (g) The absorption coefficient for the hybrid absorber. The solid curves for panels e, f, and g are calculated from Equation 30, with  $d = 21.7$  mm,  $\varpi = 1.286 \times 10^{-9}(\text{m}^2 \cdot \text{s}^3)/\text{kg}$ ,  $\hat{\omega} = 2\pi \times 162.3$  Hz, and  $\beta = 5.14$  Hz. The open circles in panel g are experimental data adapted from Ma et al. (26).

**3.6.1. Multiple scatterings and emergence of a new resonance.** As shown in **Figure 7a**, in the air layer between the dipole (DM) and the reflecting wall, there can be two sets of multiply scattered waves: one set going right and the other set going left. These multiply scattered waves can be superimposed to form two counterpropagating waves:  $p_+^i$  and  $p_+^o$ . We would like to know what would be the impedance of the DM if total absorption were to occur. With this knowledge, one can ask whether such impedance condition can be realized in practice.

For total absorption, there should be no reflection on the incident side, so conservation of  $p_m$  yields  $p_-^i = p_+^o - p_+^i$ , which may be represented by a phasor diagram (as shown in **Figure 7b**) that is an isosceles triangle, with  $p_+^i$  and  $p_+^o$  being the two equal sides with an angle  $2\delta = 2k_0d$  and  $p_-^i$  being the base. Here the angle  $2\delta$  is set by the requirement that there be a node at the reflecting wall, and hence  $p_+^i$  and  $p_+^o$  must have a relative phase of  $2\delta$  at the backside of the DM. The phasor diagram makes clear that the net pressure applied to the dipole,  $\Delta p = p_-^i - (p_+^i + p_+^o)$ , is given by  $\Delta p = p_-^i(1 - i \cot \delta)$ . It follows that the DM impedance for achieving total absorption is

$$Z = \Delta p / \bar{v} = Z_0(1 - i \cot \delta). \quad 27.$$

For  $\delta = \pi/2$ , we have  $Z = Z_0$ . Such a condition occurs at the first Fabry-Pérot (FP) resonance of the sealed cell when  $d = \lambda/4$ . This is the drum resonance because the membrane that seals the cavity is like the surface cover of a drum. However, for an air layer thinner than a quarter-wavelength, i.e.,  $\delta \rightarrow 0$ , the required imaginary part of  $Z$  approaches  $-i\infty$ . Such a large imaginary part of the DM impedance is necessary to cancel the impedance presented by the reflecting back surface, which is indeed possible for DM at a frequency slightly below the antiresonance frequency, as shown below. Because the impedance of the whole structure is the sum of two serial impedances of the DM and the sealed cell behind it, the net impedance of the composite structure should be  $Z_c = Z_0$ , i.e., impedance matched to that of air so that no reflection would occur. Because we must have  $\text{Im}(Z_c) = 0$ , the Green function of the composite structure,  $g_c = i/(\omega Z_c)$ , displays an imaginary part

$$\text{Im}(g_c) = \frac{1}{\omega} \frac{\text{Re}(Z_c)}{\text{Re}(Z_c)^2 + \text{Im}(Z_c)^2} \quad 28.$$

that exhibits a peak at this total absorption condition. A peak in the imaginary part of the Green function signifies a resonance mode. This is precisely the hybrid resonance, which must occur close to the antiresonance frequencies because only in the frequency ranges below the antiresonances would the imaginary part of the DM impedance approach the required  $-i\infty$ .

In what follows, we show that to satisfy Equation 27 in subwavelength thin air layers, the required resonant mode is a new mode of the DM, which resembles the profile at the antiresonance frequency, but with an enormously large magnitude of the  $\delta v(\mathbf{x})$  component.

**3.6.2. Characteristics of the hybrid resonance.** To characterize the hybrid resonance, for simplicity we consider only two relevant eigenmodes,  $u_1$  and  $u_2$  (see **Figure 7d**). By anticipating the resonance to be in the vicinity of the antiresonance frequency  $\tilde{\omega}$ , at which  $\text{Re}(g) = 0$ , the Green function in Equation 17 yields  $g \simeq 2\Xi(i\beta - \Delta\omega)$ , with

$$\Xi \equiv \sum_{n=1}^2 \frac{|\bar{u}_n|^2 \tilde{\omega}}{\rho_n(\omega_n^2 - \tilde{\omega}^2)^2}, \text{ and } \Delta\omega \equiv \tilde{\omega} - \omega. \quad 29.$$

The relevant impedance is given by

$$Z = \frac{1}{2\tilde{\omega}\Xi} \frac{\beta - i\Delta\omega}{\beta^2 + \Delta\omega^2}. \quad 30.$$

Equation 30 shows that for small  $\Delta\omega$  and  $\beta$ , the imaginary part of the impedance can be large and negative, up to  $-1/(4\tilde{\omega}\Xi\beta)$  at  $\Delta\omega = \beta$ . Therefore, total absorption for a very thin air layer between the DM and the back-reflecting surface is indeed possible. The hybrid resonance frequency is in between those of  $u_1$  and  $u_2$ . Thus, its eigenfunction profile must necessarily be the linear superposition of  $u_1$  and  $u_2$  because the eigenfunctions of the DM form a complete basis set, and the influence of other eigenfunctions, which are further away in their resonance frequencies, is negligible. In addition, because the hybrid mode is close to the antiresonance frequency, its profile must closely resemble that of the antiresonance; i.e., the surface-averaged displacement should be small, or  $\bar{u}_1/\bar{u}_2 \simeq 1$ . This follows from the fact that when the excitation frequency is in between the two resonances, both modes are excited, but with the opposite phase, as necessitated by the nature of the resonance response. In the present case,  $\bar{u}_1$  and  $\bar{u}_2$  do not exactly cancel, because the hybrid resonance frequency is not exactly at antiresonance and because the impedance matching requirement implies  $\bar{u}_1 - \bar{u}_2 = u_s$ , the air displacement of the incoming sound. These two conditions can be satisfied only when  $\bar{u}_{1,2} \gg u_s$ , so that  $1 - \bar{u}_2/\bar{u}_1 = u_s/\bar{u}_1$  is a small number; i.e., compared to its surface-averaged component  $\bar{u}$ , which matches the airborne sound displacement, the hybrid resonance has a much larger delta component  $\delta u$  (see **Figure 7d,e**).

Experiments reported in Reference 26 corroborated the existence of this hybrid resonance. By placing an aluminum-reflecting wall behind a DM (**Figure 7c**), an absorption coefficient of greater than 0.99 was observed at 152 Hz (**Figure 6g**). By using  $d = 21.7$  mm [which is inferred from the experimental data of 17 mm of SF6 gas, as the effects of the two thin gas layers should be identical if their thicknesses are scaled linearly with their adiabatic index (SF6 has an adiabatic index of 1.098, compared to 1.4 for air)],  $\Xi = 1.286 \times 10^{-9}(\text{m}^2 \cdot \text{s}^3)/\text{kg}$ ,  $\tilde{\omega} = 2\pi \times 162.3$  Hz, and  $\beta = 5.14$  Hz, the absorption spectrum predicted by Equation 30 was confirmed by experimental data, as shown in **Figure 7g**. In another experiment, reported by Romero-García et al. (35), a viscoelastic porous plate exhibited high absorption within a broadened frequency range when a rigid wall was placed behind it.

A similar mechanism works for the multiple scatterings between a monopole resonator and a reflecting wall. Romero-García et al. (35) demonstrated the total absorption of HRs on the sidewall of a tube, with the dead end being the reflective wall. They further showed that broadband absorption comprising four total absorption peaks can be achieved from four different HRs with a reflective wall placed at the back (36). By using the similar HR structures, Jiménez et al. (86) reported quasi-omnidirectional and total absorption of sound by a composite panel. Merkel et al. (34) showed that two different HRs, aligned in sequence, exhibited total absorption of the sound waves traveling in a ventilated tube, in which the back HR antiresonance played the role of a reflective wall. For waterborne sound, Leroy et al. (32) reported total absorption by monopolar motions of air bubbles embedded in soft solid, backed by a metallic hard wall. A series of other works reported analogous total absorptions for electromagnetic waves in systems consisting of a thin layer of dielectric medium sandwiched by one metallic reflective surface and a layer of patterned metallic film (87–90).

### 3.7. Sounds Absorption by Coiled-Space Structures and Helmholtz Resonators

As indicated by Equation 27, in addition to being achieved by the hybrid resonance, total absorption can be achieved by the FP resonances. Previous works have suggested that, if the FP channel is narrow enough, high absorption can be achieved through dissipation by air viscosity (1). However, because the FP resonances require one-quarter of a wavelength, at low frequencies that can be a significant scale for the absorption structure. One efficient way to reduce the scale is to coil the FP channel. Such tortuous structures have been mentioned in the context of porous media with

the tortuosity parameter. Here in the context of metamaterials, the coiled-space concept is used to slow down waves and to achieve negative refraction (14, 15, 92, 93).

For a particular coiled FP channel with length  $\ell$ , the condition that the air displacement velocity have a node at its reflecting end means that the internal velocity and pressure fields are given by

$$v(z) = -i \sin[\omega(z + \ell)\sqrt{\rho_0/B_0}]/\sqrt{\rho_0 B_0}, \quad p(z) = \cos[\omega(z + \ell)\sqrt{\rho_0/B_0}]. \quad 31.$$

For a FP channel  $n$  with length  $\ell_n$  within an array of  $N$  FP channels, the surface impedance at the channel's opening,  $z = 0$ , is given by

$$Z_n = \frac{p_n(0)A_t}{v_n(0)A_{\text{FP}}} = \frac{i}{\phi} Z_0 \cot[\omega\ell_n\sqrt{\rho_0/B_0}], \quad 32.$$

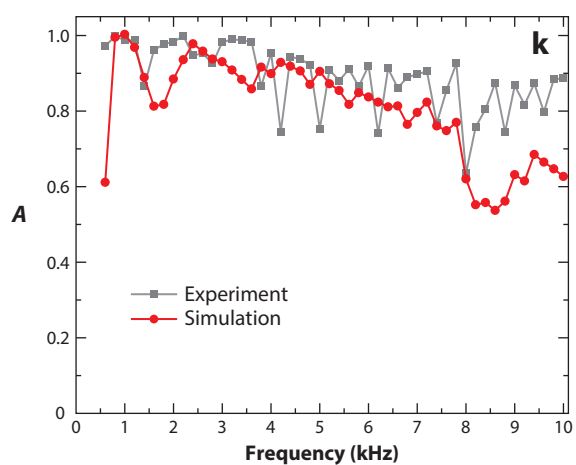
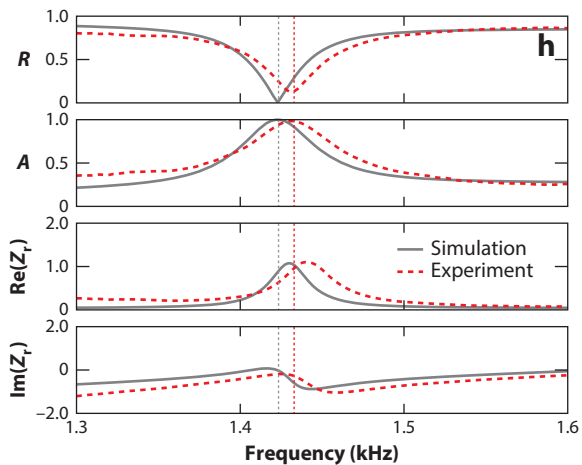
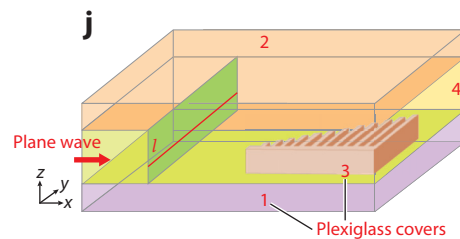
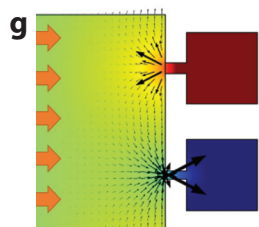
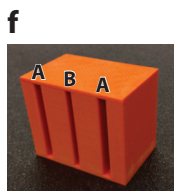
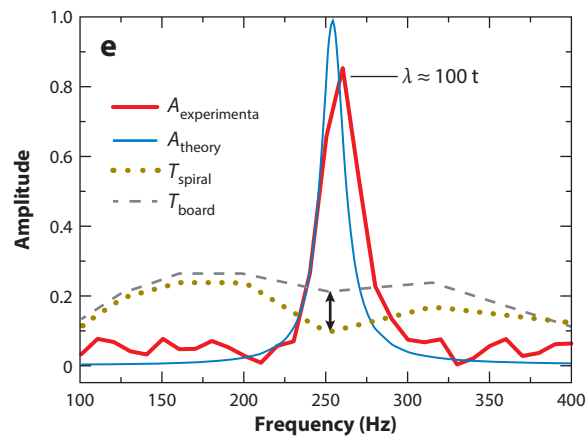
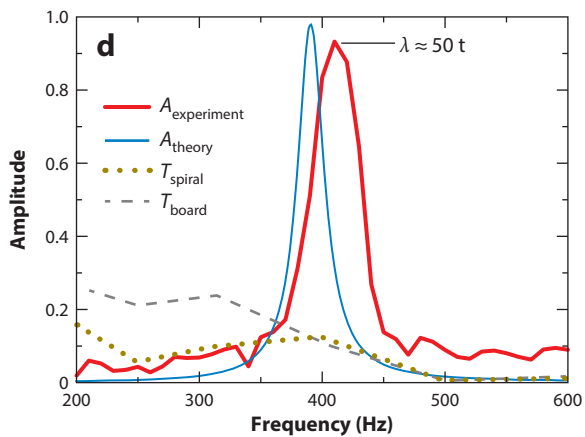
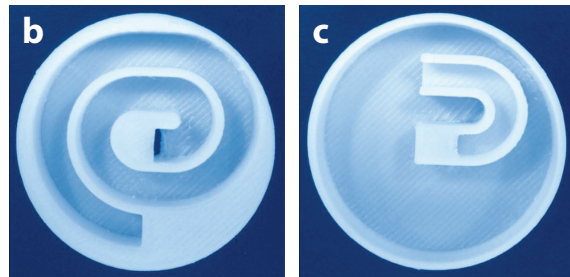
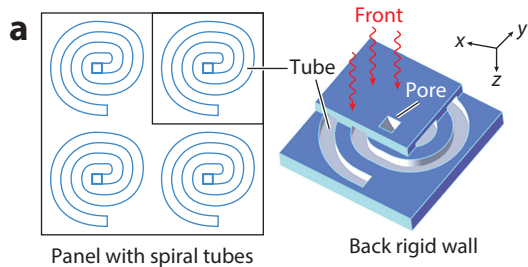
where porosity  $\phi = A_{\text{FP}}/A_t$ , with  $A_t$  being the total area of the array and  $A_{\text{FP}}$  the total area of FP channels' inner cross sections. In the present case, this ratio is exactly the porosity because  $A_{\text{FP}}$  is constant as a function of depth. Here we assume that all the  $N$  FP channels have the same cross-sectional area. To account for the small dissipation presented by air viscosity, one can simply replace  $\rho_0$  with  $\rho = (1 + 2i\beta/\omega)\rho_0$ , in which the coefficient  $\beta$  is an effective parameter characterizing air's viscosity in FP channels and its value can be obtained by fitting the experimental data (39, 39a). By Taylor expansion of the expression for  $Z_n$ , around the quarter-wavelength resonance frequency  $\Omega_n = \pi v_0/(2\ell_n)$  in Equation 32, one obtains

$$\frac{Z_n}{Z_0} \simeq i\pi \left( \frac{4\Omega_n\omega\phi/N}{\Omega_n^2 - \omega^2 - 2i\beta\omega} \right)^{-1}. \quad 33.$$

Because the FP channels are in a planar array, the total impedance of the system is given by  $Z = 1/(\sum_{n=1}^N 1/Z_n)$ . To have total absorption, this total surface impedance should match that of air; i.e.,  $Z = Z_0$ . Cai et al. (27) reported such an absorber by coiling a 205-mm FP channel into a space that is 9.7 mm thick (as shown in **Figure 8a,b**). Near-total absorption was experimentally observed at approximately 400 Hz (shown in **Figure 8d**). Subsequently, Li & Assouar (37) suggested a theoretical model based on perforated panels for similar structures. Jiang et al. (28) proposed a broadband absorber based on FP resonances that is triangular in shape, as shown in **Figure 8i,j**.

**Figure 8**

Fabry-Pérot (FP) and Helmholtz resonator (HR) absorbers. (a) Schematic drawing for an ultrathin sound absorber based on coiled FP resonant channels. (b) An image of the absorber illustrated in panel a. (c) An image of another similar absorber based on an HR that can exhibit absorption in lower frequencies. Here the horseshoe-shaped neck of the HR has an opening to the backside of the image, facing the incoming sound wave. (d) The absorption performance for the sample shown in panel b is plotted as a function of frequency. A high absorption peak is seen at approximately 400 Hz, at which the wavelength is 50 times the sample thickness. The red curve is the measured absorption coefficient, and the blue curve is the theory prediction. The dashed and dotted curves are the transmission amplitudes without and with the coiled-space structure, respectively. (e) The absorption spectrum of the sample illustrated in panel c that can absorb sound with a wavelength 100 times the sample thickness, at 250 Hz. The red curve is the measured absorption coefficient, whereas the blue curve is theory. The dashed and dotted curves are the transmission amplitude without and with the HR structure, respectively. Panels a–e adapted with permission from Cai et al. (27). (f) An image of the coupled HR absorber. (g) The simulated sound field at total absorption frequency. The orange arrows indicate the direction of incoming sounds. (h) The reflection and absorption coefficients, as well as the relevant real and imaginary parts of the normalized surface impedance  $Z_r = Z/Z_0$ , plotted as functions of frequency. The total absorption is seen at the impedance-matched frequency, with  $Z_r = 1$ . Here the solid curves are from simulations, and the red dashed curves are data. Panels f–h adapted with permission from Li et al. (91). (i) An image of a sample in which the FP resonant channels (dark colors) of various lengths are arranged in a triangular pattern. (j) A three-dimensional illustration of the sample and the measurement setup. Here 1, 2, 3, and 4 indicate plexiglass covers on four sides, forming a waveguide with a rectangular cross section with width  $l$ . (k) With FP channels resonant at different frequencies, high absorption for incoming sound was realized in a broadband frequency range. The black symbols are data, and the red symbols denote simulation results. Panels i–k adapted with permission from Jiang et al. (28).



By employing FP channels with different lengths, high absorption over a broadband frequency range was achieved, as shown in **Figure 8k**.

Another efficient way to reduce resonators' spatial scale is by utilizing the narrow-neck HR, a resonator that can be understood simply as a cavity covered by an effective mass representing the neck port and its surrounding panel (1). This effective mass corresponds with that shown in Equation 13 (with  $m_e = iZ/\omega$ ) for perforated panels. A smaller porosity  $\phi$ , implying a narrower neck of the HR, can effect a larger effective mass and therefore requires a smaller cavity for a given resonance frequency. In the experiment of Cai et al. (27), a 13.3-mm-thick HR showed a near-total absorption peak at 250 Hz (as shown in **Figure 8b,e**). In the work of Kim et al. (94), based on a theoretical model utilizing mutual radiation impedance for calculating an HR array, a high-absorption band comprising multiple peaks of HR absorption was experimentally realized. Li et al. (91) reported that, coupled through local fields, two different HRs can exhibit a hybrid resonance that absorbs sound completely (as shown in **Figure 8f-b**). Wu et al. (95) designed a split-tube resonator, comprising an HR with a coiled neck, that exhibited total absorption of sound.

#### 4. CAUSALITY CONSTRAINT AND OPTIMALITY

In traditional sound-absorbing materials/structures, the absorption spectrum is usually fixed by the thickness of the structure and cannot be easily altered. For metamaterial absorbers, however, the absorption spectrum can be tuned through structural design, even though it is usually narrow-frequency band in character. A natural question is therefore: What is the best absorption performance one can achieve over a designated frequency band, with the minimum structural thickness? The causal nature of the acoustic response offers a useful perspective with which to answer this question. Moreover, in conjunction with metamaterial design, the causality constraint can delineate the optimal sound-absorbing structure for achieving the best possible absorption performance within a designated frequency band and with the minimum thickness. A design strategy for attaining such structures is described below.

##### 4.1. Causal Nature of the Acoustic Response and the Thickness Constraint

Material response functions for electromagnetic and acoustic waves must satisfy the causality principle (96, pp. 265–67). Consider a layer of material backed by a reflecting wall. In response to an incident sound wave, the reflected sound modulation pressure,  $p_r(t)$ , is a superposition of the direct reflection of the incoming sound pressure on the interface at this instant,  $p_i(t)$ , and the reflection in response to the incident wave at an earlier time,  $p_i(t - \tau)$ , with  $\tau > 0$ . Hence

$$p_r(t) = \int_0^\infty K(\tau)p_i(t - \tau)d\tau, \quad 34.$$

where  $K(\tau)$  is the response kernel in the time domain. Through Fourier transform  $p_{i/r}(\omega) = \int_{-\infty}^\infty p_{i/r}(t)e^{i\omega t} dt$ , the reflection coefficient for each frequency may be expressed as

$$R(\omega) \equiv \frac{p_r(\omega)}{p_i(\omega)} = \int_0^\infty K(\tau)e^{i\omega\tau} d\tau. \quad 35.$$

From Equation 35,  $R(\omega)$  is an analytic function of complex  $\omega$  in the upper half of the complex  $\omega$  plane. In terms of the wavelength  $\lambda = 2\pi v_0/\omega$ , that means  $R(\lambda)$  is without singularities in the lower half-plane of complex  $\lambda$  but may have zeros that represent total absorptions of incoming energy. Here the imaginary part of  $\lambda$  signifies dissipation.

For electromagnetic waves, the causal nature of the material response function results in an inequality that relates a given absorption performance to the sample thickness (97, 98). Adapted

to acoustics, this relation (for sound waves propagating in air) can be expressed in the following form for a flat absorbing material (or structure) with thickness  $d$  sitting on a reflecting substrate:

$$d \geq \frac{1}{4\pi^2} \frac{B_{\text{eff}}}{B_0} \left| \int_0^\infty \ln[1 - A(\lambda)] d\lambda \right| = d_{\text{min}}, \quad 36.$$

where  $\lambda$  denotes the sound wavelength in air,  $A(\lambda)$  is the absorption coefficient spectrum,  $B_{\text{eff}}$  denotes the effective bulk modulus of a sound-absorbing structure in the static limit, and  $B_0$  is the bulk modulus of air. A detailed derivation of Equation 36 is given in **Supplemental Appendix A**. We define a sound-absorbing structure to be optimal if equality or near-equality is attained in the above relation. Some obvious implications immediately follow from Equation 36. For example, 100% absorption within a finite frequency range is not possible for any finite thickness sample. Also, high absorption at low frequencies would dominate the contribution to sample thickness. However,  $A(\lambda) \sim 1$  at a particular low frequency is entirely possible for a very subwavelength sample thickness, provided that the absorption peak is narrow, as shown in Section 3.6 for hybrid resonance.

 Supplemental Material

## 4.2. Causal Optimality of Sound-Absorbing Structures

It would be interesting to assess various sound-absorbing structures' degree of causal optimality in terms of Equation 36. Take the glass wool shown in **Figure 1** as the first example. By keeping the porosity,  $\phi$ , unchanged and varying its static permeability,  $\kappa_0$ , we wish to see whether causal optimality can be achieved for a sample of glass wool that is 5.6 cm in thickness. Varying  $\kappa_0$  is equivalent to changing the cross-sectional dimension of the pores, with narrower pores leading to smaller  $\kappa_0$ . By substituting the absorption spectrum predicted by Equation 12 into Equation 36, we plot in **Figure 9a** the value of  $d_{\text{min}}$  as a function of  $\kappa_0$ . It is seen that a critical permeability  $\kappa_c$  exists below which the causal integral gives the minimum sample thickness  $d_{\text{min}}$  equal to that of the sample,  $d = 5.6$  cm. In other words, for  $\kappa_0 > \kappa_c$ , the sample thickness is always larger than  $d_{\text{min}}$ , implying that better absorption can be achieved by reducing permeability. However, if the static permeability is reduced to much below  $\kappa_c$ , then the absorption spectrum becomes more flattened; i.e., high absorption in some frequency regimes is reduced in favor of broadening the absorption spectrum.

A similar critical condition exists for the MPP whose structure is illustrated in **Figure 2**. On the basis of the absorption spectrum as predicted by Equation 13, the casual integral on the right-hand side of Equation 36 can yield a value of  $d_{\text{min}}$  as a function of pore diameter  $l$ . Here the sample is 6 cm in thickness. The results are plotted in **Figure 9e**. There is clearly a critical  $l_c$  below which causal optimality is achieved. Panels *f–h* of **Figure 9** show the absorption spectra at three different values of  $l$ . Together these spectra indicate that causal optimality does not necessarily mean high absorption. Rather, there is always a trade-off between high absorption and the bandwidth of the absorption spectrum for a fixed thickness.

As a third example, we show that metamaterial DM hybrid resonant absorbers have similar features. Here the dissipative parameter  $\beta$  is chosen to be the variable in a hybrid resonator that is 21.7 mm in thickness. In **Figure 9i**, the  $d_{\text{min}}$  as evaluated by the predicted absorption spectrum (based on Equation 30) is plotted as a function of  $\beta$ . The critical dissipative parameter is predicted to be  $\beta_c = 5.14$  Hz, which is the value for achieving perfect absorption. For  $\beta < \beta_c$ , the peak absorption is less than 1, and Equation 36 is an inequality; for  $\beta > \beta_c$ , the peak absorption is less than 1 as well, but the spectrum has a broader bandwidth so that  $d_{\text{min}} = d$ . Such behaviors are clearly seen in **Figure 9i–l**.

The above clearly shows that causal optimality does not always guarantee high absorption. Instead, there is a trade-off between the bandwidth of the absorption spectrum, the sample thickness, and the absorption coefficient. Hence to use the causality constraint to delineate the ultimate sound-absorbing structures, one must specify two out of the three parameters, with the third

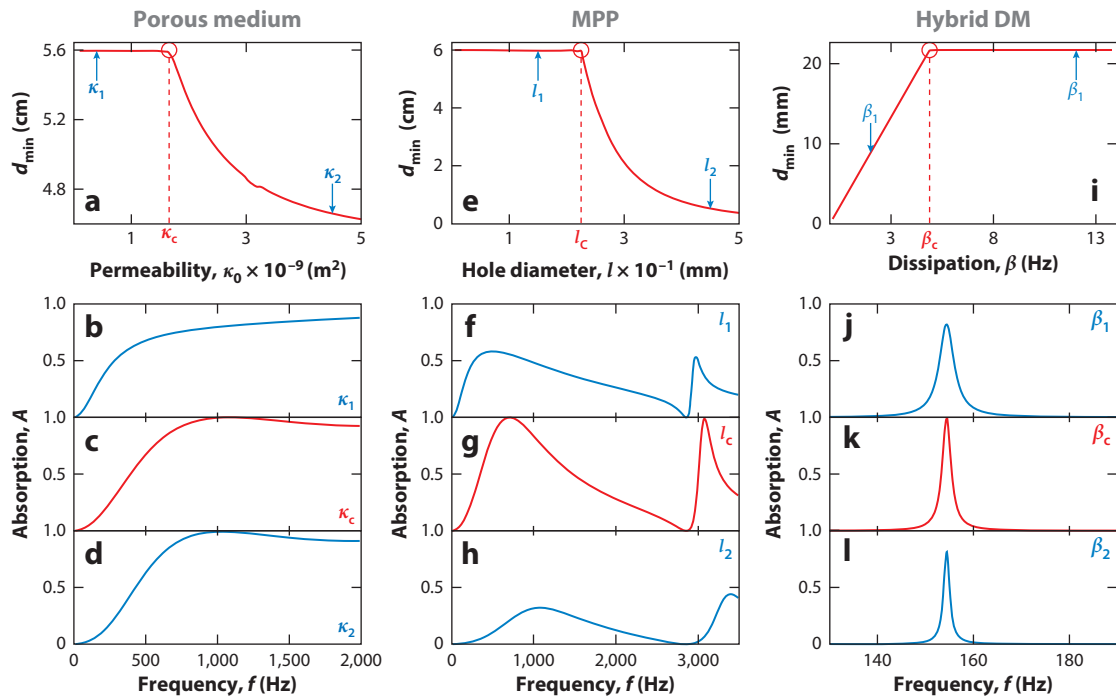


**Figure 9**

Porous and hybrid absorbers as inspected from the causal constraint perspective. (a) The minimum thickness  $d_{\min}$  as determined by the causal integral (Equation 36), in which the absorption spectrum is that predicted by Equation 12 for the porous materials shown in **Figure 1**. Here the static permeability  $\kappa_0$  is treated as a variable. The sample thickness  $d = 5.6$  cm. The other parameter values in the absorption spectra calculations are the same as those for **Figure 1**. There is a critical permeability value below which causal optimality (defined as  $d = d_{\min}$ ) is attained. (b–d) The relevant absorption spectra for the three different permeability values marked in panel a. For  $\kappa_2$ ,  $d_{\min}/d \simeq 84\%$ , and the absorption spectrum shown in panel d is only slightly lower than that shown in panel c for  $\kappa_c$ . The main difference lies in the slightly lower absorption in the low-frequency regime and in the 2,000-Hz regime. For the spectrum shown in panel b for  $\kappa_1$ , the causal integral is the same as that for  $\kappa_c$ , but low-frequency absorption is improved at the expense of higher-frequency absorption. (e) The minimum thickness  $d_{\min}$  evaluated by using the absorption spectrum based on Equation 13 for the micro-perforated panel (MPP) absorber, shown in **Figure 2** with a MPP sample thickness of 6 cm. The other parameter values in the absorption spectra calculations are the same as those for **Figure 2**. Here the hole diameters  $l$  are treated as the variable. (f–h) The absorption spectra for the three different diameters marked in panel e. For  $l_2$ , absorption is low. As the hole diameter decreases to  $l_c$ , absorption increases appreciably. With further decreases in hole diameter, the maximum absorption decreases, but absorption becomes more even distributed as a function of frequency. (i) The minimal thickness  $d_{\min}$  evaluated by using the absorption spectrum predicted by Equation 30 for the hybrid decorated membrane (DM) shown in **Figure 7**, with a sample thickness of 21.7 mm. Here the dissipation coefficient  $\beta$  is treated as the variable. (j–l) There is a critical  $\beta_c$  below which the absorption is low and beyond which the maximum drops but the absorption spectrum broadens. This is illustrated for the three values of  $\beta$  marked in panel i.

one to be optimized. To facilitate this process, the following two questions can be used, in conjunction with the causal optimality, to delineate the target optimal sound-absorbing structure. The first question is: For a target absorption spectrum,  $A(\lambda)$ , what is the minimum sample thickness required? The second is: Given a sample thickness, what is the structure that can achieve the best absorption performance over a given frequency band? The following section describes a custom-designed strategy for achieving the target absorption spectrum with the minimum allowed thickness. The same strategy can be used, with some additional optimization techniques, to achieve the goal set by the second question.

## 5. DESIGN STRATEGY FOR ATTAINING OPTIMAL SOUND-ABSORBING STRUCTURES

Because traditional sound-absorbing materials cannot offer the freedom to tune the absorption frequency spectrum, realizing an optimal sound-absorbing structure as defined by the above two questions must involve acoustic metamaterials in the design strategy. Below we describe such a strategy (39, 39a) and the example of realizing broadband absorption, with near-perfect absorption starting at a low-frequency cutoff, by using a designed acoustic material as backing to a thin layer of a traditional sound-absorbing material, such as an acoustic sponge.

### 5.1. Theoretical Basis for a Custom-Designed Strategy

Similar to that for DM as shown in Equation 17, the impedance for an acoustic metamaterial with multiple resonances is given by  $Z = i/(\omega g)$ , or

$$Z = \frac{i\rho_0 d}{\omega} \left( \sum_n \frac{\alpha_n}{\Omega_n^2 - \omega^2 - 2i\beta\omega} \right)^{-1}. \quad 37.$$

Here  $\rho_0$  is the density of air;  $\omega$  is the angular frequency;  $\Omega_n$  denotes the  $n$ th resonance frequency;  $\alpha_n$  is its dimensionless oscillator strength, given by  $\alpha_n = 4d\phi\Omega_n/(N\pi v_0)$  for FP channels so as to be consistent with Equation 33; and  $\beta \ll \omega$  describes the weak system dissipation for the acoustic metamaterial. For Equation 37 to be accurate, the lateral size of the metamaterial units (if they are assumed to be periodically arranged) must be very subwavelength in scale so that the diffraction effects can be neglected.

To design an absorber structure for a target absorption spectrum,  $A(\omega)$ , placed against a reflecting surface, let us consider an idealized case in which resonances have a continuum distribution with mode density  $D(\omega)$  per unit frequency. In that case, Equation 37 can be converted to an integral,

$$Z \simeq \lim_{\beta \rightarrow 0} \frac{i\rho_0 d}{\omega} \left( \int_{\Omega_1}^{\infty} \frac{\alpha(\Omega)D(\Omega)}{\Omega^2 - \omega^2 - 2i\beta\omega} d\Omega \right)^{-1}. \quad 38.$$

We have set a lower cutoff for the integral,  $\Omega_1$ , so as to exclude the zero frequency from our consideration. The oscillatory nature of the real part of the integrand in Equation 38 implies that the integrated result approaches zero very quickly for  $\omega > \Omega_1$ . Hence for the design strategy, only the imaginary part is considered. By defining  $\mu(\Omega) = \alpha(\Omega)D(\Omega)$ , then

$$\lim_{\beta \rightarrow 0} \text{Im} \left[ \frac{\mu(\Omega)}{\Omega^2 - \omega^2 - 2i\omega\beta} \right] = \lim_{\beta \rightarrow 0} \frac{2\omega\beta\mu(\Omega)}{4\omega^2\beta^2 + (\omega^2 - \Omega^2)^2} = \pi\mu(\Omega)\delta(\omega^2 - \Omega^2), \quad 39.$$

with  $\delta(\omega^2 - \Omega^2)$  being the Dirac delta function. Equation 38 can be converted into

$$Z \simeq \frac{\rho_0 d}{\pi\omega} \left[ \int_0^{\infty} \mu(\Omega)\delta(\omega^2 - \Omega^2)d\Omega \right]^{-1} = \frac{2\rho_0 d}{\pi\mu(\omega)}, \quad 40.$$

or

$$\mu(\omega) = \alpha(\omega)D(\omega) = \frac{2\rho_0 d}{\pi Z(\omega)}. \quad 41.$$

Because by definition  $D(\omega) = \Delta n / \Delta\omega$ , i.e., the number of modes within a frequency range  $\Delta\omega$ , Equation 41 can be expressed as a differential equation for the mode distribution  $\Omega(n)$ :

$$\frac{d\Omega}{dn} = \frac{\pi\alpha(\Omega)Z(\Omega)}{2\rho_0 d}, \quad 42.$$

where  $n$  is treated as a continuous variable. By further substituting  $\alpha = 4d\phi\Omega/(N\pi v_0)$  into Equation 42 for FP channels, we obtain

$$\frac{d\Omega}{dn} = \frac{2\phi}{N} \frac{Z(\Omega)}{Z_0} \Omega. \quad 43.$$

This differential equation can be solved with the initial condition  $\Omega = \Omega_1$  at  $n = 1$ , in conjunction with the input  $Z(\omega)$  obtained from the target absorption spectrum  $A(\omega)$  for  $\omega > \Omega_1$ ; i.e.,

$$Z(\omega) = Z_0 \left[ 2 - A(\omega) + 2\sqrt{1 - A(\omega)} \right] / A(\omega). \quad 44.$$

To be specific, we choose FP  $\lambda/4$  resonators to realize the designed structure. For an array of FP channels, the mode distribution inherently implies a minimum thickness of the sample because  $\Omega_n = \pi v_0 / (2\ell_n)$ , and by volume conservation the minimum thickness of the sample is given by  $\bar{d} = \phi \sum_{n=1}^N \ell_n / N$ , provided that each channel's cross section is the same. Requiring  $\bar{d} = d_{\min}$  as evaluated from Equation 36 leads to a unique value of  $\phi$ . This is shown explicitly in the example below.

## 5.2. Idealized Model for Realizing a Broadband Optimal Metamaterial Absorber

For a BOMA, the desired target impedance is flat in frequency and is close to the air impedance  $Z_0 = \rho_0 v_0$  starting at a lower cutoff frequency  $\Omega_1$ . From Equation 41, that means  $\mu = 2\rho_0 d / (\pi Z_0)$  for  $\omega > \Omega_1$  and  $\mu = 0$  for  $\Omega < \Omega_1$ . With this condition, Equation 38 can be evaluated to yield

$$Z = \frac{\pi Z_0}{\pi - 2i \tanh^{-1}(\Omega_1/\omega)}. \quad 45.$$

**Figure 10a** shows the behavior for the real and imaginary parts of  $Z$ . The imaginary part, owing to the oscillatory nature of the integrand in Equation 38, rapidly decays to zero for  $\omega > \Omega_1$ , as noted above. The real part of the impedance approaches the impedance-matching condition  $Z/Z_0 = 1$

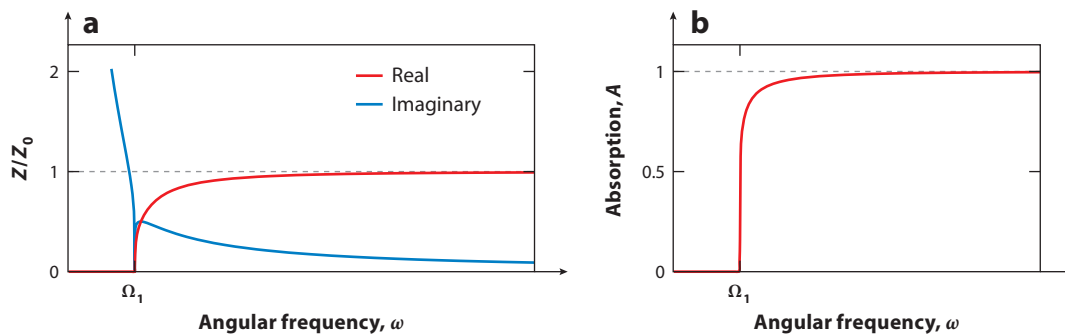


**Figure 10**

Idealized broadband optimal metamaterial absorber with continuously distributed resonance frequencies above a cutoff  $\Omega_1$ . (a) The relevant surface impedance is plotted as a function of frequency. Here the imaginary part vanishes quickly above the cutoff frequency  $\Omega_1$ , whereas the real part of the impedance approaches the air impedance. (b) The relevant sound absorption coefficient is plotted as a function of frequency. Above the cutoff, the absorption coefficient is very close to 1 but does not reach 1, as it is constrained by the causality relation. Also, above the cutoff frequency, only the square of the imaginary part of the impedance enters the absorption coefficient. Hence the small nonzero  $\text{Im}(Z)$ 's effect on absorption is even smaller than that indicated in panel a.

beyond  $\Omega_1$ . The absorption spectrum can be calculated by using the formula

$$A = 1 - \left| \frac{(Z/Z_0) - 1}{(Z/Z_0) + 1} \right|^2 = 1 - \left| \frac{\tanh^{-1}(\Omega_1/\omega)}{\pi - i \tanh^{-1}(\Omega_1/\omega)} \right|^2. \quad 46.$$

The absorption predicted by Equation 46 is plotted in **Figure 10b**. In this idealized case, the acoustic metamaterial is sufficient to achieve near-perfect broadband absorption, requiring only an infinitesimal dissipation coefficient. By substituting  $A(\lambda)$  as expressed by Equation 46 into Equation 36, with  $\lambda = 2\pi v_0/\omega$  and  $B_{\text{eff}} = B_0$ , we obtain  $d \geq 2v_0/(\pi\Omega_1) = d_{\text{min}}$ . The lesson from this idealized case is that flat impedance as a function of frequency requires the mode density to be inversely proportional to the oscillator strength; i.e.,  $\mu$  should be frequency independent.

## 6. REALIZATION OF BROADBAND ABSORBERS WITH DISCRETE ARRAYS OF RESONATORS

To realize a BOMA with a lower-frequency cutoff as delineated by the idealized model, Yang et al. (39, 39a) reported a cuboid structure comprising 16 tightly folded FP channels each with a square cross section that is  $\sim 1.038$  cm on the side, separated from each other with a 1-mm-thick wall; hence porosity  $\phi = 0.85$ . The folding, designed by computer simulations, can be seen for the channels shown in **Figure 11a**. In that case, the average channel length is given by  $\bar{d} = 10.58$  cm. In the actual sample with folded channels, the cuboid has a thickness of  $d = 11.06$  cm. As shown in **Figure 12b**, with a 1-cm sponge in front of the metamaterial unit, such an absorber structure can achieve near-equality in the casual relation (Equation 36), with a flat, near-perfect absorption spectrum starting at 400 Hz. In particular, the right-hand side of Equation 36 yields 11.5 cm, whereas the actual sample thickness is 12 cm. If the channel folding can be improved so that the limit of  $\bar{d} = 10.58$  cm is reached, then the total thickness would be 11.58 cm; i.e., Equation 36 would essentially become an equality. Details on how this is achieved are briefly given below.

### 6.1. Surface Response of Metamaterials with Discrete Resonances

To design the first-order resonance frequencies of the FP channels, we set  $\Omega_1 = 2\pi \times 372.8$  Hz to be the lowest resonance frequency, with the resonance frequency of each channel increasing with increasing  $n$ . By solving Equation 43 with  $Z(\Omega)/Z_0$  set equal to 1, we obtain  $\Omega_n = \Omega_1 \exp[2\phi(n-1)/N]$ . **Figure 11b** shows the relevant  $\alpha_n$  for the 11 of  $N = 16$  resonance frequencies with  $\Omega_{16} = 2\pi \times 1,835$  Hz.

Because the first-order FP resonance frequency of the  $n$ th channel is given by  $\Omega_n = \pi v_0/(2\ell_n)$ , we have  $\ell_n = \pi v_0 \exp[2\phi(1-n)/N]/(2\Omega_1)$ , and

$$\bar{d} = \lim_{N \rightarrow \infty} \frac{\phi}{N} \sum_{n=1}^N \ell_n = \frac{\pi v_0}{4\Omega_1} (1 - e^{-2\phi}). \quad 47.$$

By requiring  $\bar{d} = d_{\text{min}} = 2v_0/(\pi\Omega_1)$  evaluated from the causality constraint, for BOMA, there is an optimal value for  $\phi$  given by

$$\phi = -\frac{1}{2} \log \left( 1 - \frac{8}{\pi^2} \right) = 0.832. \quad 48.$$

This value is closely approached by the actual sample with  $\phi = 0.85$ .

**Figure 11c** shows the measured impedance of the designed metamaterial unit. The measured impedances oscillate around  $Z_0$  with peaks and valleys. This oscillation is expected because there

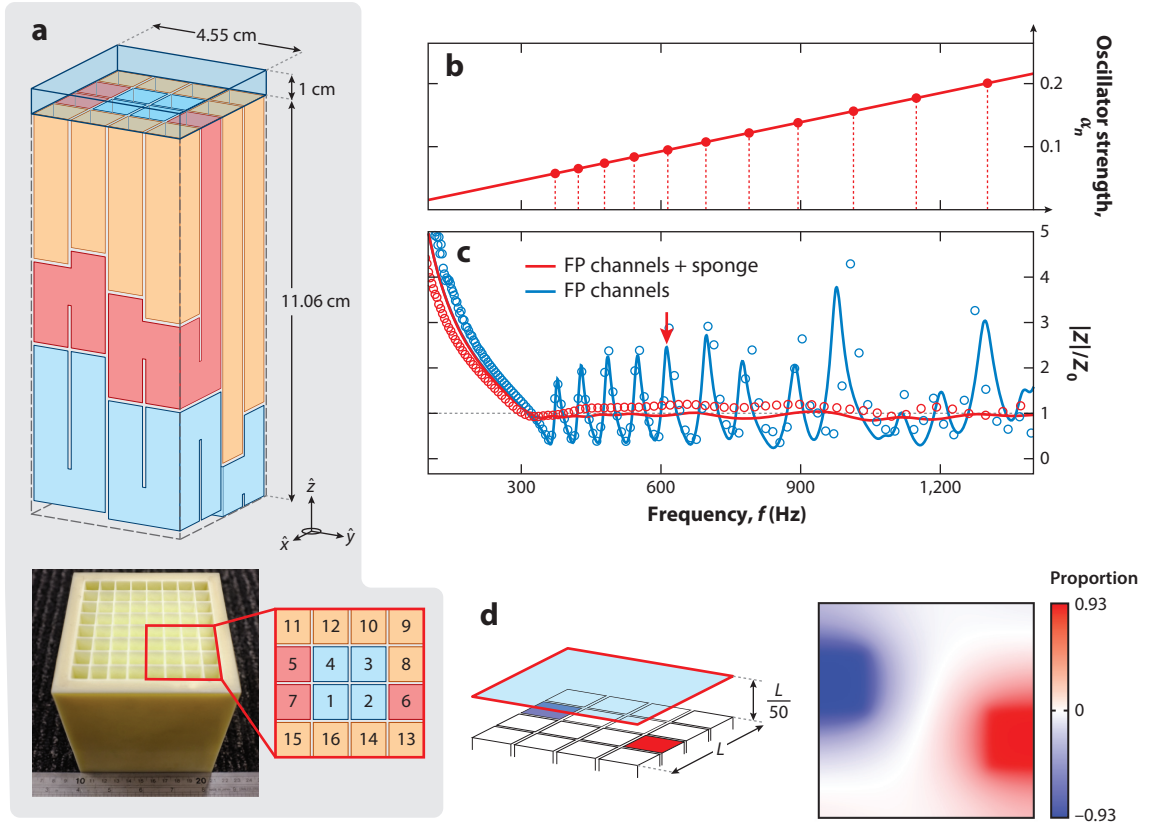


**Figure 11**

The structure and features of the broadband optimal metamaterial absorber. (a) Schematic illustration of the metamaterial unit consisting of 16 Fabry-Pérot (FP) channels, arrayed in a  $4 \times 4$  square lattice, with the longer FP channels folded to form a compact, cuboid sample. The channel's number denotes its order in the sequence of decreasing lengths. Blue channels are coiled by three foldings, pink channels are coiled by two foldings, and the orange channels are straight. The transparent cyan block represents the sponge to be placed on top of the channels' surface. An image of the unit is shown in the lower left panel. (b) Eleven of the 16 oscillator-strength  $\alpha_n$  of the FP channels'  $\lambda/4$  resonances, plotted as a function of frequency. The frequency positions are designed in accordance with the solution to Equation 43. (c) The measured (open circles) and calculated (solid lines) surface impedance of the metamaterial unit,  $Z_{\text{bare}}$  (blue), and that with a 1-cm-thick sponge placed on top (red). The theory predictions are based on Equation 53, in which the red curve was calculated by replacing  $\rho_0$  with  $\rho_{\text{sponge}}$ . (d) The evanescent wave is illustrated by showing sound pressures at 0.91 mm above the front surface of the metamaterial, obtained by simulation at 610 Hz (the position is indicated by the red arrow in panel c). This frequency coincides with the antiresonance frequency between the FP resonances of the fifth and sixth channels (blue and red squares, respectively).

are 16 discrete resonances, and the impedance peaks can be associated with the antiresonances that are in between the neighboring resonances. By treating each FP channel to be independent from others and in parallel with each other, the impedance of the unit, denoted by  $Z_{\text{bare}}$ , can be written as

$$Z_{\text{bare}} = \frac{i}{\omega} \left( \frac{1}{16} \sum_{n=1}^{16} g_n \right)^{-1}, \quad 49.$$

with  $g_n = \tan(\omega \ell \sqrt{\rho_0/B_0})/(\omega Z_0)$ .  $Z_{\text{bare}}$  displays oscillations in a similar fashion as the measured results. However, if a 1-cm layer of acoustic sponge is placed on top of the unit, then the impedance

is shown as in **Figure 11c**. The oscillations almost completely vanish. In the following, we show that the origin of this effect is due to the evanescent waves that laterally couple the  $v_n$ s at the mouths of different FP channels and the waves' interaction with a highly dissipative medium.

## 6.2. Impedance Renormalization by Evanescent Waves

For sound with a wavelength  $\lambda$  much larger than the metamaterial unit's cross-sectional scale  $L$ , the impedance measured at far field is given by  $Z = \bar{p}/\bar{v}$ , where  $\bar{v} = \sum_{n=1}^{16} v_n/16$ . However, locally we must have

$$v_n = -i\omega g_n(\bar{p} + \delta p_n), \quad 50.$$

where  $\delta p_n$  represents the value of  $\delta p(\mathbf{x})$  at the  $n$ th FP channel location. We note that  $\sum_{n=1}^{16} \delta p_n = 0$ , yet  $\sum_{n=1}^{16} g_n \delta p_n \neq 0$ . Therefore, lateral inhomogeneity can clearly contribute to the renormalization of the bare impedance. Under a uniformly applied pressure  $\bar{p}$  on the surface, the response  $v_n$  consists of two parts: One part is  $-i\omega g_n \bar{p}$ , and the other part is the response arising from evanescent waves; i.e.,

$$v_n = -i\omega \left( g_n + \frac{\omega^2 \rho_0 g_n^2 \Lambda_{nn}}{1 - \omega^2 \rho_0 g_n \Lambda_{nn}} + \sum_m \Pi_{nm} \right) \bar{p}. \quad 51.$$

There is a relationship between  $\delta p_n$  and  $v_n$ , derived in **Supplemental Appendix B**:

$$\delta p_n = i\omega \rho_0 \sum_m \Lambda_{nm} v_m, \quad 52a.$$

$$\Lambda_{nm} = 16 \sum_\alpha \frac{\sin^2(\alpha_x \pi/4) \sin^2(\alpha_y \pi/4)}{\pi^4 \alpha_x^2 \alpha_y^2 |\mathbf{k}_\alpha|} \times \exp[i\mathbf{k}_\alpha \cdot (\mathbf{x}_m - \mathbf{x}_n)], \quad 52b.$$

with  $\mathbf{x}_n$  being the coordinate of the center of the  $n$ th channel at its mouth,  $\delta p_n = \delta p(\mathbf{x}_n)$ ,  $v_m = v(\mathbf{x}_m)$ , and  $|\mathbf{k}_\alpha| = (2\pi/L)\sqrt{\alpha_x^2 + \alpha_y^2} \gg 2\pi/\lambda$  with  $\alpha_x, \alpha_y = \pm 1, \pm 2, \dots$ . In Equation 51, the first term in the parentheses represents the bare response of the metamaterial, and the rest of the terms represent the effects arising from evanescent waves. The last term is from the coupling between different channels through evanescent waves, which is much weaker than the second term. By summing over  $n$  on both sides of the equation, the renormalized impedance is given by

$$Z = (1/Z_{\text{bare}} + 1/\delta Z)^{-1}, \quad 53a.$$

with

$$\delta Z = \frac{16i}{\omega} \left( \sum_n \frac{\omega^2 \rho_0 g_n^2 \Lambda_{nn}}{1 - \omega^2 \rho_0 g_n \Lambda_{nn}} + \sum_n \sum_m \Pi_{nm} \right)^{-1}. \quad 53b.$$

The resonance of the independent FP channels is identifiable by the frequencies at which  $g_n$ s diverge. From Equation 51 and the definition of impedance, the renormalized resonances should be at those frequencies that yield divergence of the coefficient in front of  $\bar{p}$ . If we add together the first two terms inside the parentheses of Equation 51 and ignore the small contributions from  $\Pi_{nm}$ , the result is a renormalized Green function given by

$$g_n^{(e)} = \frac{1}{g_n^{-1} - \omega^2 \rho_0 \Lambda_{nn}}; \quad 54.$$

hence the resonance should occur at a frequency slightly below  $\Omega_n$ , where the real part of  $g_n^{-1} = \omega^2 \rho_0 \Lambda_{nn}$ . **Figures 11c** and **12a** show that the predictions of Equation 53 can give an excellent quantitative account of the experimental results.

 Supplemental Material

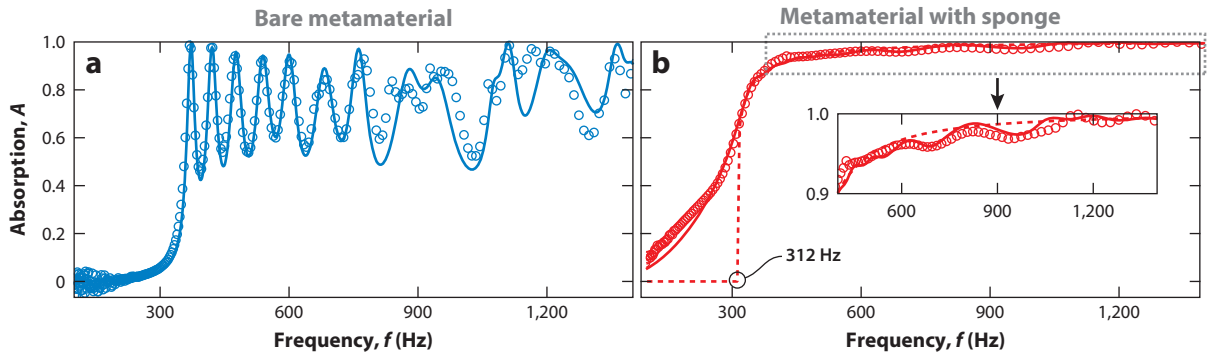


**Figure 12**

Absorption behavior of the designed broadband optimal metamaterial absorber. (a) The absorption spectrum of the bare metamaterial unit with 16 Fabry-Pérot channels. The spectrum is choppy, an inherent characteristic for metamaterials comprising multiple, discrete resonances. The open circles are measured data, and the solid line denotes the theory prediction based on Equation 53, with the relevant parameter values given in the text. (b) The absorption for the metamaterial unit with a 1-cm sponge covering in front. The solid curve is the theoretical prediction based on Equation 53, with  $\rho_0$  replaced with  $\rho_{\text{sponge}}$ , which has an imaginary dissipative component that is two orders of magnitude larger than that for  $\rho_0$ . The rather flat and near-perfect absorption spectrum is the combined result of impedance renormalization by the evanescent waves, plus their interaction with a high dissipative medium. Such an effect was previously observed and qualitatively explained for a profiled acoustic diffuser structure (99). For comparison, the absorption spectrum of the idealized case is delineated by the dashed lines (see **Figure 10**). Panels *a* and *b* adapted from References 39 and 39a.

By adding a layer of acoustic sponge in front of the metamaterial, the air density  $\rho_0$  should be replaced with the effective density of sponge  $\rho_{\text{sponge}}$  in Equation 54. Because  $\rho_{\text{sponge}}$  has a very large imaginary part, the renormalized resonances become highly damped so that, at both the resonances and antiresonances of the combined system, the real part of  $\sum_{n=1}^{16} g_n^{(e)}/16$  is zero, leaving only a nonzero imaginary part. As a result, there is a positive real part for  $Z$  that is nearly flat as a function of frequency, owing to the designed mode density rule discussed above.

By setting  $\beta = 7.1$  Hz in Equation 49, the renormalized impedance with Equation 53b predicts the surface impedance and absorption for a bare metamaterial sample (see **Figure 12a**). To predict the absorption spectrum of the combined sample, comprising a 1-cm sponge in front of the designed metamaterial, the effective density of the sponge was set as  $\rho_{\text{sponge}} = [1.4 + i(1,420\text{Hz})/\omega]\rho_0$  (following Equation 9). The results are shown in **Figure 12b**, which indeed displays good agreement with the target spectrum as derived from the idealized model and with the theory prediction based on Equations 53 and 54.

## 7. CONCLUDING REMARKS AND OUTLOOK

This review surveys sound-absorbing structures ranging from conventional materials with porous microstructures to acoustic metamaterials and to the most recently reported structures designed by custom-set targets. The role of constraints imposed by geometry, symmetry, and causality is especially emphasized, as such constraints determine what is attainable. Further development of sound-absorbing structures should push these boundaries by altering the basis of the constraints. Such developments could involve, for example, changing the nature of the absorbing structures from passive to a combination of passive and active or altering the geometric and symmetry of the structures to fit some particular applications. The phase space of the possibilities is enormous in terms of opportunities for basic research and applications, and one can only be optimistic about future developments.

## DISCLOSURE STATEMENT

The authors are not aware of any affiliations, memberships, funding, or financial holdings that might be perceived as affecting the objectivity of this review.

## ACKNOWLEDGMENTS

This study was supported by AoE/P-02/12.

## LITERATURE CITED

1. Allard J, Atalla N. 2009. *Propagation of Sound in Porous Media: Modelling Sound Absorbing Materials*. Chichester, UK: John Wiley & Sons. 2nd ed.
2. Sagartzazu X, Hervella-Nieto L, Pagalday J. 2008. Review in sound absorbing materials. *Arch. Comput. Methods Eng.* 15:311–42
3. Liu Z, Zhang X, Mao Y, Zhu Y, Yang Z, et al. 2000. Locally resonant sonic materials. *Science* 289:1734–36
4. Fang N, Xi D, Xu J, Ambati M, Srituravanich W, et al. 2006. Ultrasonic metamaterials with negative modulus. *Nat. Mater.* 5:452–56
5. Lee SH, Park CM, Seo YM, Wang ZG, Kim CK. 2010. Composite acoustic medium with simultaneously negative density and modulus. *Phys. Rev. Lett.* 104:054301
6. Lai Y, Wu Y, Sheng P, Zhang ZQ. 2011. Hybrid elastic solids. *Nat. Mater.* 10:620–24
7. Wu Y, Lai Y, Zhang ZQ. 2011. Elastic metamaterials with simultaneously negative effective shear modulus and mass density. *Phys. Rev. Lett.* 107:105506
8. Yang M, Ma G, Yang Z, Sheng P. 2013. Coupled membranes with doubly negative mass density and bulk modulus. *Phys. Rev. Lett.* 110:134301
9. Brunet T, Merlin A, Mascaro B, Zimny K, Leng J, et al. 2015. Soft 3D acoustic metamaterial with negative index. *Nat. Mater.* 14:384–88
10. Cummer SA, Christensen J, Alù A. 2016. Controlling sound with acoustic metamaterials. *Nat. Rev. Mater.* 1:16001
11. Ma G, Sheng P. 2016. Acoustic metamaterials: from local resonances to broad horizons. *Sci. Adv.* 2:e1501595
12. Xie Y, Wang W, Chen H, Konneker A, Popa BI, Cummer SA. 2014. Wavefront modulation and sub-wavelength diffractive acoustics with an acoustic metasurface. *Nat. Commun.* 5:5553
13. Li Y, Jiang X, Liang B, Cheng J, Zhang L. 2015. Metascreen-based acoustic passive phased array. *Phys. Rev. Appl.* 4:024003
14. Liang Z, Li J. 2012. Extreme acoustic metamaterial by coiling up space. *Phys. Rev. Lett.* 108:114301
15. Xie Y, Popa BI, Zigoneanu L, Cummer SA. 2013. Measurement of a broadband negative index with space-coiling acoustic metamaterials. *Phys. Rev. Lett.* 110:175501
16. Kaina N, Lemoult F, Fink M, Lerosey G. 2015. Negative refractive index and acoustic superlens from multiple scattering in single negative metamaterials. *Nature* 525:77–81
17. Li J, Fok L, Yin X, Bartal G, Zhang X. 2009. Experimental demonstration of an acoustic magnifying hyperlens. *Nat. Mater.* 8:931–34
18. Zhu J, Christensen J, Jung J, Martin-Moreno L, Yin X, et al. 2011. A holey-structured metamaterial for acoustic deep-subwavelength imaging. *Nat. Phys.* 7:52–55
19. Christensen J, de Abajo FJG. 2012. Anisotropic metamaterials for full control of acoustic waves. *Phys. Rev. Lett.* 108:124301
20. Zigoneanu L, Popa BI, Cummer SA. 2014. Three-dimensional broadband omnidirectional acoustic ground cloak. *Nat. Mater.* 13:352–55
21. Faure C, Richoux O, Félix S, Pagneux V. 2016. Experiments on metasurface carpet cloaking for audible acoustics. *Appl. Phys. Lett.* 108:064103
22. Liang B, Guo X, Tu J, Zhang D, Cheng J. 2010. An acoustic rectifier. *Nat. Mater.* 9:989–92
23. Fleury R, Sounas DL, Sieck CF, Haberman MR, Alù A. 2014. Sound isolation and giant linear nonreciprocity in a compact acoustic circulator. *Science* 343:516–19

24. Yang M, Li Y, Meng C, Fu C, Mei J, et al. 2015. Sound absorption by subwavelength membrane structures: a geometric perspective. *C. R. Méc.* 343:635–44
25. Mei J, Ma G, Yang M, Yang Z, Wen W, Sheng P. 2012. Dark acoustic metamaterials as super absorbers for low-frequency sound. *Nat. Commun.* 3:756
26. Ma G, Yang M, Xiao S, Yang Z, Sheng P. 2014. Acoustic metasurface with hybrid resonances. *Nat. Mater.* 13:873–78
27. Cai X, Guo Q, Hu G, Yang J. 2014. Ultrathin low-frequency sound absorbing panels based on coplanar spiral tubes or coplanar Helmholtz resonators. *Appl. Phys. Lett.* 105:121901
28. Jiang X, Liang B, Li R-q, Zou X-y, Yin L-l, Cheng J-c. 2014. Ultra-broadband absorption by acoustic metamaterials. *Appl. Phys. Lett.* 105:243505
29. Wei P, Croënne C, Chu ST, Li J. 2014. Symmetrical and anti-symmetrical coherent perfect absorption for acoustic waves. *Appl. Phys. Lett.* 104:121902
30. Song J, Bai P, Hang Z, Lai Y. 2014. Acoustic coherent perfect absorbers. *New J. Phys.* 16:033026
31. Duan Y, Luo J, Wang G, Hang ZH, Hou B, et al. 2015. Theoretical requirements for broadband perfect absorption of acoustic waves by ultra-thin elastic meta-films. *Sci. Rep.* 5:12139
32. Leroy V, Strybulevych A, Lanoy M, Lemoult F, Tourin A, Page JH. 2015. Superabsorption of acoustic waves with bubble metascreens. *Phys. Rev. B* 91:020301
33. Yang M, Meng C, Fu C, Li Y, Yang Z, Sheng P. 2015. Subwavelength total acoustic absorption with degenerate resonators. *Appl. Phys. Lett.* 107:104104
34. Merkel A, Theocharis G, Richoux O, Romero-García V, Pagneux V. 2015. Control of acoustic absorption in one-dimensional scattering by resonant scatterers. *Appl. Phys. Lett.* 107:244102
35. Romero-García V, Theocharis G, Richoux O, Merkel A, Tournat V, Pagneux V. 2016. Perfect and broadband acoustic absorption by critically coupled sub-wavelength resonators. *Sci. Rep.* 6:19519
36. Romero-García V, Theocharis G, Richoux O, Pagneux V. 2016. Use of complex frequency plane to design broadband and sub-wavelength absorbers. *J. Acoust. Soc. Am.* 139:3395–403
37. Li Y, Assouar BM. 2016. Acoustic metasurface-based perfect absorber with deep subwavelength thickness. *Appl. Phys. Lett.* 108:063502
38. Meng C, Zhang X, Tang ST, Yang M, Yang Z. 2016. Acoustic coherent perfect absorbers as sensitive null detectors. arXiv:1610.03749 [physics.class-ph]
39. Yang M, Chen S, Fu C, Sheng P. 2016. Optimal sound absorbing structures. arXiv:1609.09561 [physics.class-ph]
- 39a. Yang M, Chen S, Fu C, Sheng P. 2017. Optimal sound absorbing structures. *Mater. Horiz.* <https://doi.org/10.1039/c7mh00129k>
40. Allard JF, Depollier C, Guignouard P, Rebillard P. 1991. Effect of a resonance of the frame on the surface impedance of glass wool of high density and stiffness. *J. Acoust. Soc. Am.* 89:999–1001
41. Landau L, Lifshitz E. 2004. *Fluid Mechanics*, Vol. 6. Oxford, UK: Butterworth-Heinemann. 2nd ed.
42. Champoux Y, Stinson MR, Daigle GA. 1991. Air-based system for the measurement of porosity. *J. Acoust. Soc. Am.* 89:910–16
43. Whitaker S. 1986. Flow in porous media. I. A theoretical derivation of Darcy's law. *Transp. Porous Media* 1:3–25
44. Carman PC. 1956. *Flow of Gases Through Porous Media*. London: Butterworth
45. Johnson DL, Koplik J, Dashen R. 1987. Theory of dynamic permeability and tortuosity in fluid-saturated porous media. *J. Fluid Mech.* 176:379–402
46. Kostek S, Schwartz LM, Johnson DL. 1992. Fluid permeability in porous media: comparison of electrical estimates with hydrodynamical calculations. *Phys. Rev. B* 45:186–95
47. Johnson DL, Koplik J, Schwartz LM. 1986. New pore-size parameter characterizing transport in porous media. *Phys. Rev. Lett.* 57:2564–67
48. Champoux Y, Allard JF. 1991. Dynamic tortuosity and bulk modulus in air-saturated porous media. *J. Appl. Phys.* 70:1975–79
49. Von Terzaghi K. 1923. Die Berechnung der Durchlässigkeit des Tones aus dem Verlauf der hydromechanischen Spannungserscheinungen. *Sitzungsber. Akad. Wiss. Math. Naturwiss. Kl. Abt. IIa* 182:125–38
50. Biot MA. 1941. General theory of three-dimensional consolidation. *J. Appl. Phys.* 12:155–64

51. Biot MA. 1956. Theory of deformation of a porous viscoelastic anisotropic solid. *J. Appl. Phys.* 27:459–67
52. Biot MA. 1956. Theory of propagation of elastic waves in a fluid-saturated porous solid. I. Low-frequency range. *J. Acoust. Soc. Am.* 28:168–78
53. Biot MA. 1956. Theory of propagation of elastic waves in a fluid-saturated porous solid. II. Higher frequency range. *J. Acoust. Soc. Am.* 28:179–91
54. Delany M, Bazley E. 1970. Acoustical properties of fibrous absorbent materials. *Appl. Acoust.* 3:105–16
55. Allard JF, Champoux Y. 1992. New empirical equations for sound propagation in rigid frame fibrous materials. *J. Acoust. Soc. Am.* 91:3346–53
56. Lafarge D, Nematı N. 2013. Nonlocal Maxwellian theory of sound propagation in fluid-saturated rigid-framed porous media. *Wave Motion* 50:1016–35
57. Nematı N, Lafarge D. 2014. Check on a nonlocal Maxwellian theory of sound propagation in fluid-saturated rigid-framed porous media. *Wave Motion* 51:716–28
58. Maa DY. 1998. Potential of microperforated panel absorber. *J. Acoust. Soc. Am.* 104:2861–66
59. Bolt RH. 1947. On the design of perforated facings for acoustic materials. *J. Acoust. Soc. Am.* 19:917–21
60. Callaway D, Ramer L. 1952. The use of perforated facings in designing low frequency resonant absorbers. *J. Acoust. Soc. Am.* 24:309–12
61. Ingard U. 1953. On the theory and design of acoustic resonators. *J. Acoust. Soc. Am.* 25:1037–61
62. Ingard U. 1954. Perforated facing and sound absorption. *J. Acoust. Soc. Am.* 26:151–54
63. Morse PM, Ingard KU. 1968. *Theoretical Acoustics*. New York: McGraw Hill
64. Maa DY. 1975. Theory and design of microperforated panel sound-absorbing constructions. *Sci. Sin.* 18:55–71
65. Raleigh JWD. 1929. *Theory of Sound. II*. New York: MacMillan. 327 pp.
66. Crandall IB. 1926. *Theory of Vibration System and Sound*. New York: Van Nostrand. 229 pp.
67. Liu J, Herrin D. 2010. Enhancing micro-perforated panel attenuation by partitioning the adjoining cavity. *Appl. Acoust.* 71:120–27
68. Wang C, Huang L. 2011. On the acoustic properties of parallel arrangement of multiple micro-perforated panel absorbers with different cavity depths. *J. Acoust. Soc. Am.* 130:208–18
69. Wang C, Huang L, Zhang Y. 2014. Oblique incidence sound absorption of parallel arrangement of multiple micro-perforated panel absorbers in a periodic pattern. *J. Sound Vib.* 333:6828–42
70. Park SH. 2013. Acoustic properties of micro-perforated panel absorbers backed by Helmholtz resonators for the improvement of low-frequency sound absorption. *J. Sound Vib.* 332:4895–911
71. Yang Z, Mei J, Yang M, Chan N, Sheng P. 2008. Membrane-type acoustic metamaterial with negative dynamic mass. *Phys. Rev. Lett.* 101:204301
72. Yang M, Ma G, Wu Y, Yang Z, Sheng P. 2014. Homogenization scheme for acoustic metamaterials. *Phys. Rev. B* 89:064309
73. Bliokh KY, Bliokh YP, Freilikher V, Savelev S, Nori F. 2008. Unusual resonators: plasmonics, metamaterials, and random media. *Rev. Mod. Phys.* 80:1201–13
74. Xu Y, Li Y, Lee RK, Yariv A. 2000. Scattering-theory analysis of waveguide-resonator coupling. *Phys. Rev. E* 62:7389–404
75. Chen Y, Huang G, Zhou X, Hu G, Sun CT. 2014. Analytical coupled vibroacoustic modeling of membrane-type acoustic metamaterials: membrane model. *J. Acoust. Soc. Am.* 136:969–79
76. Chen Y, Huang G, Zhou X, Hu G, Sun CT. 2014. Analytical coupled vibroacoustic modeling of membrane-type acoustic metamaterials: plate model. *J. Acoust. Soc. Am.* 136:2926–34
77. Ivansson SM. 2012. Anechoic coatings obtained from two-and three-dimensional monopole resonance diffraction gratings. *J. Acoust. Soc. Am.* 131:2622–37
78. Wen J, Zhao H, Lv L, Yuan B, Wang G, Wen X. 2011. Effects of locally resonant modes on underwater sound absorption in viscoelastic materials. *J. Acoust. Soc. Am.* 130:1201–208
79. Meng H, Wen J, Zhao H, Lv L, Wen X. 2012. Analysis of absorption performances of anechoic layers with steel plate backing. *J. Acoust. Soc. Am.* 132:69–75
80. Achilleos V, Richoux O, Theocharis G. 2016. Coherent perfect absorption induced by the nonlinearity of a Helmholtz resonator. arXiv:1601.03912 [physics.class-ph]
81. Godwin R. 1972. Optical mechanism for enhanced absorption of laser energy incident on solid targets. *Phys. Rev. Lett.* 28:85–87

82. Freidberg J, Mitchell R, Morse RL, Rudsinski L. 1972. Resonant absorption of laser light by plasma targets. *Phys. Rev. Lett.* 28:795–99
83. Kindel J, Lee K, Lindman E. 1975. Surface-wave absorption. *Phys. Rev. Lett.* 34:134–38
84. Yang M, Ma G, Yang Z, Sheng P. 2015. Subwavelength perfect acoustic absorption in membrane-type metamaterials: a geometric perspective. *EPJ Appl. Metamater.* 2:10
85. Piper JR, Liu V, Fan S. 2014. Total absorption by degenerate critical coupling. *Appl. Phys. Lett.* 104:251110
86. Jiménez N, Huang W, Romero-García V, Pagneux V, Groby JP. 2016. Ultra-thin metamaterial for perfect and quasi-omnidirectional sound absorption. *Appl. Phys. Lett.* 109:121902
87. Landy N, Sajuyigbe S, Mock J, Smith D, Padilla W. 2008. Perfect metamaterial absorber. *Phys. Rev. Lett.* 100:207402
88. Ye D, Wang Z, Xu K, Li H, Huangfu J, et al. 2013. Ultrawideband dispersion control of a metamaterial surface for perfectly-matched-layer-like absorption. *Phys. Rev. Lett.* 111:187402
89. Radi Y, Simovski C, Tretyakov S. 2015. Thin perfect absorbers for electromagnetic waves: theory, design, and realizations. *Phys. Rev. Appl.* 3:037001
90. Lee YP, Rhee JY, Yoo YJ, Kim KW. 2016. Broadband and tunable MMPA. In *Metamaterials for Perfect Absorption*, ed. Y Pak Lee, JY Rhee, YJ Yoo, KW Kim, pp. 113–41. Singapore: Springer
91. Li J, Wang W, Xie Y, Popa BI, Cummer SA. 2016. A sound absorbing metasurface with coupled resonators. *Appl. Phys. Lett.* 109:091908
92. Liang Z, Feng T, Lok S, Liu F, Ng KB, et al. 2013. Space-coiling metamaterials with double negativity and conical dispersion. *Sci. Rep.* 3:1614
93. Xie Y, Konneker A, Popa BI, Cummer SA. 2013. Tapered labyrinthine acoustic metamaterials for broadband impedance matching. *Appl. Phys. Lett.* 103:201906
94. Kim S, Kim YH, Jang JH. 2006. A theoretical model to predict the low-frequency sound absorption of a Helmholtz resonator array. *J. Acoust. Soc. Am.* 119:1933–36
95. Wu X, Fu C, Li X, Meng Y, Gao Y, et al. 2016. Low-frequency tunable acoustic absorber based on split tube resonators. *Appl. Phys. Lett.* 109:043501
96. Landau L, Lifshitz E, Pitaevskii L. 1995. *Electrodynamics of Continuous Media*, Vol. 8. Oxford, UK: Butterworth-Heinemann. 2nd ed.
97. Fano RM. 1950. Theoretical limitations on the broadband matching of arbitrary impedances. *J. Franklin Inst.* 249:57–83
98. Rozanov KN. 2000. Ultimate thickness to bandwidth ratio of radar absorbers. *IEEE Trans. Antennas Propag.* 48:1230–34
99. Wu T, Cox T, Lam Y. 2000. From a profiled diffuser to an optimized absorber. *J. Acoust. Soc. Am.* 108:643–50
200. Fahy F. 2001. *Foundations of Engineering Acoustics*. London: Academic



# Contents

## Novel Functionality Through Metamaterials (Venkatraman Gopalan, Don Lipkin & Simon Phillpot, Editors)

Control of Localized Surface Plasmon Resonances in Metal Oxide Nanocrystals <i>Ankit Agrawal, Robert W. Johns, and Delia J. Milliron</i> .....	1
DNA-Driven Assembly: From Polyhedral Nanoparticles to Proteins <i>Martin Girard, Jaime A. Millan, and Monica Olvera de la Cruz</i> .....	33
Harnessing Instabilities to Design Tunable Architected Cellular Materials <i>Katia Bertoldi</i> .....	51
Negative-Poisson's-Ratio Materials: Auxetic Solids <i>Roderic S. Lakes</i> .....	63
Sound Absorption Structures: From Porous Media to Acoustic Metamaterials <i>Min Yang and Ping Sheng</i> .....	83
Structured X-Ray Optics for Laboratory-Based Materials Analysis <i>Carolyn A. MacDonald</i> .....	115
Synchrotron X-Ray Optics <i>Albert T. Macrander and XianRong Huang</i> .....	135

## Current Interest

Active Crystal Growth Techniques for Quantum Materials <i>Julian L. Schmeyer and Stephen D. Wilson</i> .....	153
Atomic-Scale Structure-Property Relationships in Lithium Ion Battery Electrode Materials <i>Zhenzhong Yang, Lin Gu, Yong-Sheng Hu, and Hong Li</i> .....	175
Atomistic Simulations of Activated Processes in Materials <i>G. Henkelman</i> .....	199

Deformation of Crystals: Connections with Statistical Physics <i>James P. Sethna, Matthew K. Bierbaum, Karin A. Dahmen, Carl P. Goodrich, Julia R. Greer, Lorien X. Hayden, Jaron P. Kent-Dobias, Edward D. Lee, Danilo B. Liarte, Xiaoyue Ni, Katherine N. Quinn, Archbishopman Raju, D. Zeb Rocklin, Ashvini Shekhawat, and Stefano Zapperi</i> .....	217
Heusler 4.0: Tunable Materials <i>Lukas Wollmann, Ajaya K. Nayak, Stuart S.P. Parkin, and Claudia Felser</i> .....	247
Physical Dynamics of Ice Crystal Growth <i>Kenneth G. Libbrecht</i> .....	271
Silicate Deposit Degradation of Engineered Coatings in Gas Turbines: Progress Toward Models and Materials Solutions <i>David L. Poerschke, R. Wesley Jackson, and Carlos G. Levi</i> .....	297
Structural and Functional Fibers <i>Huibin Chang, Jeffrey Luo, Prabhakar V. Gulgunje, and Satish Kumar</i> .....	331
Synthetic Two-Dimensional Polymers <i>Marco Servalli and A. Dieter Schlüter</i> .....	361
Transparent Perovskite Barium Stannate with High Electron Mobility and Thermal Stability <i>Woong-Jhae Lee, Hyung Joon Kim, Jeonghun Kang, Dong Hyun Jang, Tai Hoon Kim, Jeong Hyuk Lee, and Kee Hoon Kim</i> .....	391
Visualization of Atomic-Scale Motions in Materials via Femtosecond X-Ray Scattering Techniques <i>Aaron M. Lindenberg, Steven L. Johnson, and David A. Reis</i> .....	425
X-Ray Tomography for Lithium Ion Battery Research: A Practical Guide <i>Patrick Pietsch and Vanessa Wood</i> .....	451

## Indexes

Cumulative Index of Contributing Authors, Volumes 43–47 .....	481
---	-----

## Errata

An online log of corrections to *Annual Review of Materials Research* articles may be found at <http://www.annualreviews.org/errata/matsci>